Title page

Decoding multiple zoning patterns in clinopyroxene phenocrysts at Vulcano Island: A record of dynamic crystallization through interconnected reservoirs

[1]Flavia Palummo, [1,2]Silvio Mollo, [3]Chiara Maria Petrone, [4]Ben S. Ellis, [2]Gianfilippo De Astis, [2]Manuela Nazzari, [2]Piergiorgio Scarlato, [4]Olivier Bachmann

[1]Department of Earth Sciences, Sapienza - University of Rome, P. le Aldo Moro 5, 00185 Roma, Italy

[2]Istituto Nazionale di Geofisica e Vulcanologia - Department Roma 1, Via di Vigna Murata 605, 00143 Roma, Italy

[3]The Natural History Museum, Department of Earth Sciences, Cromwell Road, SW7 5BD, London, United Kingdom

[4]Institute of Geochemistry and Petrology, ETH Zürich, 8092 Zurich, Switzerland

Corresponding author:

Flavia Palummo

Sapienza-Università di Roma

Dipartimento di Scienze della Terra

P.le Aldo Moro 5

00185 Roma, Italy

e-mail flavia.palummo@uniroma1.it

Abstract

Here we document how the different growth features and intracrystalline distributions of both major and trace cations in clinopyroxene phenocrysts are important recorders of the intricate magma dynamics at Vulcano Island (Aeolian Arc, Italy). The compositions of clinopyroxene phenocrysts from products erupted over the last ~54 ka cluster at different degrees of evolution, paralleling the polybaric-polythermal differentiation of mantle-derived mafic magmas into more evolved silicic melts. The hotter lower crust is the most favorable location for the storage of mafic magmas and the early crystallization of diopsidic ($Mg\#_{91}$) clinopyroxene (P_{max} ≈ 750 MPa and T_{max} ≈ 1,220 °C). Diopsidic phenocrysts are depleted in both rare earth elements (REE) and high field strength elements (HFSE) but are enriched in transition elements (TE). The transfer and accumulation of primitive magmas in the colder upper crustal regions lead to the formation of an interconnected series of more differentiated magmatic reservoirs (P ≈ 100-450 MPa and T ≈ 1,100-1,180 °C) hosting discrete populations of clinopyroxene ($Mg\#_{84-85}$) with a broad spectrum of zonations and dissolution features. Recharge bands in clinopyroxene are markers of multiple inputs of primitive REE-HFSE-poor, TE-rich magmas from depth. Augitic phenocrysts ($Mg\#_{82}$) with strong negative Eu anomaly and REE + HFSE enrichments crystallizes from highly differentiated trachytic and rhyolitic melts stored at very shallow crustal conditions (P ≤ 50 MPa and T ≤ 1,100 °C). These silicic reservoirs represent residual melts trapped-extracted from crystal-dominated mush regions in the uppermost part of the plumbing system. The residence time of clinopyroxene increases from ~0.1 to ~44 years from basalt to rhyolite, together with an increasing number of recharge bands. The mineral assemblage in more silicic and viscous mush melts is sufficiently resilient to record numerous mafic injections and high degrees of magma mixing, hybridization, and crystallization before eruption. Overall, the compositional zoning pattern of clinopyroxene presents a picture of plumbing system that extends through the crust and is

characterized by distributions of melts and crystals which are progressively more evolved and heterogeneous in both space and time.

Research Highlights

Clinopyroxene erupted at Volcano Island over the last ~54 ka have been studied

Clinopyroxene records magma mixing/hybridization/crystallization phenomena

Clinopyroxene heterogeneity is exacerbated in crystal-dominated mush zones

Clinopyroxene residence time increases with melt differentiation

Decoding multiple zoning patterns in clinopyroxene phenocrysts at Vulcano Island: A record of dynamic crystallization through interconnected reservoirs

[1]Flavia Palummo, [1,2]Silvio Mollo, [3]Chiara Maria Petrone, [4]Ben S. Ellis, [2]Gianfilippo De Astis, [2]Manuela Nazzari, [2]Piergiorgio Scarlato, [4]Olivier Bachmann

[1]Department of Earth Sciences, Sapienza - University of Rome, P. le Aldo Moro 5, 00185 Roma, Italy

[2]Istituto Nazionale di Geofisica e Vulcanologia - Department Roma 1, Via di Vigna Murata 605, 00143 Roma, Italy

[3]The Natural History Museum, Department of Earth Sciences, Cromwell Road, SW7 5BD, London, United Kingdom

[4]Institute of Geochemistry and Petrology, ETH Zürich, 8092 Zurich, Switzerland

Corresponding author:

Flavia Palummo

Sapienza-Università di Roma

Dipartimento di Scienze della Terra

P.le Aldo Moro 5

00185 Roma, Italy

e-mail flavia.palummo@uniroma1.it

Abstract

Here we document how the different growth features and intracrystalline distributions of both major and trace cations in clinopyroxene phenocrysts are important recorders of the intricate magma dynamics at Vulcano Island (Aeolian Arc, Italy). The compositions of clinopyroxene phenocrysts from products erupted over the last ~54 ka cluster at different degrees of evolution, paralleling the polybaric-polythermal differentiation of mantle-derived mafic magmas into more evolved silicic melts. The hotter lower crust is the most favorable location for the storage of mafic magmas and the early crystallization of diopsidic ($Mg\#_{91}$) clinopyroxene (P_{max} ≈ 750 MPa and T_{max} ≈ 1,220 °C). Diopsidic phenocrysts are depleted in both rare earth elements (REE) and high field strength elements (HFSE) but are enriched in transition elements (TE). The transfer and accumulation of primitive magmas in the colder upper crustal regions lead to the formation of an interconnected series of more differentiated magmatic reservoirs (P ≈ 100-450 MPa and T ≈ 1,100-1,180 °C) hosting discrete populations of clinopyroxene ($Mg\#_{84-85}$) with a broad spectrum of zonations and dissolution features. Recharge bands in clinopyroxene are markers of multiple inputs of primitive REE-HFSE-poor, TE-rich magmas from depth. Augitic phenocrysts ($Mg\#_{82}$) with strong negative Eu anomaly and REE + HFSE enrichments crystallizes from highly differentiated trachytic and rhyolitic melts stored at very shallow crustal conditions (P ≤ 50 MPa and T ≤ 1,100 °C). These silicic reservoirs represent residual melts trapped-extracted from crystal-dominated mush regions in the uppermost part of the plumbing system. The residence time of clinopyroxene increases from ~0.1 to ~44 years from basalt to rhyolite, together with an increasing number of recharge bands. The mineral assemblage in more silicic and viscous mush melts is sufficiently resilient to record numerous mafic injections and high degrees of magma mixing, hybridization, and crystallization before eruption. Overall, the compositional zoning pattern of clinopyroxene presents a picture of plumbing system that extends through the crust and is

characterized by distributions of melts and crystals which are progressively more evolved and heterogeneous in both space and time.

Keywords: clinopyroxene; Vulcano Island; magma dynamics; magma mixing, hybridization, and crystallization; plumbing system architecture.

1. Introduction

Vulcano Island (Aeolian Arc, Italy) is characterized by a broad spectrum of clinopyroxene-bearing eruptive products, with a general temporal variation in compositions from basalt to rhyolite (e.g., Keller, 1980; Ellam et al., 1988; De Astis et al., 1997, 2013). The volcanic history is controlled by the continuous supply of mafic magma from mantle depths into shallow crustal levels, where high degrees of mixing and fractional crystallization lead to the formation of more differentiated reservoirs, together with occasional assimilation of small amounts of crustal materials (Bullock et al., 2019; Costa et al., 2020, 2021; De Astis et al., 1997; Gioncada et al., 1998, 2003; Forni et al., 2015; Nicotra et al., 2018; Palummo et al., 2020; Peccerillo et al., 2006; Piochi et al., 2009; Zanon et al., 2003).

The picture emerging from geophysical, volcanological, and petrological considerations is entirely consistent with a plumbing system that extends vertically through the crust and is characterized by a multi-faceted geometry (Clocchiatti et al., 1994; De Astis et al., 1997, 2013; Peccerillo et al., 2006; Zanon et al., 2003; Costa et al., 2020, 2021; Nicotra et al., 2018; Palummo et al., 2020). Considering this articulated architecture, we infer that complex zoning patterns in clinopyroxene phenocrysts have the potential to integrate a broad range of spatio-temporal information, providing an important record of the physico-chemical changes of magmas (Forni et al., 2016; Mollo et al., 2015, 2020a; Szymanowski et al., 2016; Ubide et al., 2019a; Welsch et al., 2016;). Clinopyroxene is an important recorder of mixing, hybridization, and differentiation mechanisms that control the dynamics of magma within the crust and, ultimately, preserves a detailed record of the magma recharge history (Di Stefano et al., 2020; Dunworth et al., 2001; Gioncada et al., 2005; Mangler et al., 2020; Tecchiato et al., 2018; Ubide et al., 2019b). Deconvolution of systematic zoning patterns in clinopyroxene may help to reconstruct the recharge dynamics of magma reservoirs, as well as the time and length scales required to mobilize magmas before eruptions (e.g., Petrone et al., 2016, 2018; Ubide and Kamber, 2018). Additionally, the stability field of clinopyroxene encompasses a broad range of *P-T-X* conditions, from mantle depths to very shallow crustal levels, and its crystallization may strictly control the geochemical evolution of solidifying melts in terms of major and trace element contents (e.g., Beard et al., 2019; Masotta et al., 2013; Mollo and Masotta, 2014; Mollo et al., 2015; Putirka et al., 2008; Perinelli et al., 2016; Sun and Liang, 2012, 2017).

Although the investigation of clinopyroxene complexity and diversity can be a powerful tool to gain information on the dynamics of multi-stage plumbing systems, no studies have yet categorized and decoded the complex zoning patterns of clinopyroxene at Vulcano Island. For this purpose, we present a broad compositional data set for major and trace elements analyzed in clinopyroxene phenocrysts from twenty-one basaltic-to-rhyolitic products representative of the volcanism occurred from ~54 ka to historical times. A detailed petrological description, geochemical modeling, and petrogenetic significance of fifteen products with ages in the range of ~8-54 ka can be found in Palummo et al. (2020). Here the data set has been integrated with six latitic and trachytic rock samples, which extend the eruptive period to the youngest product of La Fossa cone dated at 1739 CE on the basis of contemporary historical chronicles (see De Astis et al., 2013 and references therein). Interrogation of the textural and compositional changes of clinopyroxene reveals that zonations are intrinsic to the process of magma solidification, thus providing a more comprehensive view of the geochemical evolution of multiple magma batches undergoing polybaric-polythermal crystallization under open-system conditions. The interpretation and modeling of major and trace cation distributions in clinopyroxene affords considerable insight into the mechanisms and timescales by which multiple magma storage regions developed at variable depths and then interacted with each other, before feeding volcanic eruptions.

2. Volcanological background

Vulcano Island is an active volcanic system located in the southernmost sector of the Aeolian Archipelago (Fig. 1a), a Quaternary volcanic arc generated by subduction of the oceanic Ionian plate underneath the Calabrian arc (Ventura, 2013). The Aeolian Archipelago consists of seven islands and nine seamounts forming a ring-like structure, whose northwestern sector lies on the oceanic crust of the Tyrrhenian abyssal plain and eastern and southern sectors on ~18-25 km thick continental crust of the Calabro-Peloritano basement (De Astis et al., 1997). The three islands of Vulcano, Lipari, and Salina are part of a volcanic complex that developed within a graben-like structure controlled by the NNW-SSE strike-slip Tindari–Letojanni fault system (Gioncada et al., 2003; Ventura, 2013). Accordingly, the structural pattern of Vulcano Island is dominated by major NW–SE- to NNW–SSE-striking fault system (De Astis et al., 2013). The island has a total surface area of ~22 km^2, its base lies at an average depth of ~1 km b.s.l. and the maximum height is ~499 m a.s.l. at Monte Aria (De Astis et al., 2013 and references therein). The calc-alkaline affinity of the erupted products is related to subduction processes due to the presence of a NW-dipping Benioff-Wadati zone (Davì et al., 2009). The subaerial volcanic activity at Vulcano Island started 127 ka in the southern sector of the island with the building of Primordial Vulcano stratocone (Fig. 1a; Mandarano et al., 2016). Afterwards, the volcanic edifice was affected by volcano-tectonic collapses occurring at 100, 80, and 50 ka. The first two collapses were related to the formation of Il Piano caldera, whereas the third collapse was associated to the early phases of La Fossa caldera (Fig. 1a; Davì et al., 2009). The last eruption occurred from August 1888 to March 1890 at La Fossa cone (Keller, 1980). This is a 391-m-high tuff cone mainly developed through phreatomagmatic eruptions and minor lava effusions (Dellino et al., 2011). The peninsula of Vulcanello (Fig. 1a) formed as a new islet in Roman times. This peninsula represents the northernmost structure located along the northern border of La Fossa caldera, consisting of a lava platform and three nested scoria cones with alignment ENE-WSW (Davì et al., 2009; De Astis et al., 1997, 2013). According to De Astis et al. (2013), the overall eruptive history of Vulcano Island can be divided in eight Eruptive Epochs (Fig. 1a) that represent the principal building stages of the volcanic edifice interrupted by periods of quiescence, sometimes also associated with volcano-tectonic collapses (e.g., Il Piano Caldera, La Fossa Caldera).

3. Sampling and analytical methods

3.1. Sample selection

The magmatic activity of the last ~54 ka at Vulcano Island has been investigated through textural and chemical (major and trace elements) analyses of clinopyroxene phenocrysts (i.e., crystals with longest size dimensions >0.3 mm; Lanzafame et al., 2013 and references therein) from various volcanic rocks, mainly lavas and scoriae, erupted during the considered timespan.

A total of twenty-one rock samples, were collected from several strategic sectors and formations, in which the eruptive units were identified on the basis of their different lithostratigraphic and compositional characteristics (Table 1). The rock samples represent the last Eruptive Epochs 5, 6, 7, and 8 (i.e., between ~54 ka and 1739 CE; De Astis et al., 2013) of Vulcano Island (Fig. 1a). According to the TAS diagram (Total Alkali vs. Silica; Le Bas et al., 1986; Fig. 1b), samples are classified as five distinct groups: 1) basalts ($SiO_2 \approx$ 48.9-51.4 wt.%; $Na_2O + K_2O \approx$ 4.3-4.6 wt.%), 2) basaltic trachyandesites (i.e., shoshonites; $SiO_2 \approx$ 52.2-54.4 wt.%; $Na_2O + K_2O \approx$ 7.3-7.9 wt.%), 3) trachyandesites (i.e., latites; $SiO_2 \approx$ 54.2-57.5 wt.%; $Na_2O + K_2O \approx$ 7.1-9.2 wt.%), 4) trachytes ($SiO_2 \approx$ 62.4-68.4 wt.%; $Na_2O + K_2O \approx$ 8.3-9.1 wt.%) and 5) rhyolites ($SiO_2 \approx$ 71.0-73.7 wt.%; $Na_2O + K_2O \approx$ 8.5-8.7 wt.%). Bulk rock analyses of rock samples and a detailed description of their eruptive epochs are reported in Supplementary Material 1.

3.2. Analytical methods

Textural and chemical microanalyses on clinopyroxene phenocrysts were carried out with a field emission gun-scanning electron microscope (FE-SEM) and an electron microprobe (EMP), respectively, installed at the High Pressure - High Temperature (HP-HT) Laboratory of Experimental Volcanology and Geophysics of the Istituto Nazionale di Geofisica e Vulcanologia (INGV) in Rome (Italy). Trace element analyses of clinopyroxene phenocrysts were determined by laser ablation-inductively coupled plasma-mass spectrometry (LA-ICP-MS) at the Institute of

Geochemistry and Petrology, ETH Zürich (Switzerland). Conditions used for analyses are reported in Supplementary Material 1.

4. Results

4.1. Clinopyroxene textural and chemical zonation

Clinopyroxene is the ubiquitous mineral phase in all the investigated samples and usually the length of its longest axis is comprised between 0.3 and 1 mm. Distinctive and complex textural changes are observed for clinopyroxene by combining grey level distribution of high-contrast BSE (backscattered electron) images (Fig. 2) and X-ray microprobe maps in false colors (Fig. 3). On this basis, five main clinopyroxene populations have been identified (Table 1):

- Type 1: unzoned phenocrysts. Euhedral phenocrysts with homogeneous compositions are extremely rare in the erupted products (Fig. 2). Unzoned phenocrysts are prevalently found in basalts and some primitive shoshonites, whereas they are absent in latites, trachytes and rhyolites (Table 1);
- Type 2: cores/resorbed cores. Several phenocryst cores are heralds of an early stage of crystallization and one or more resorbed cores preserve evidence of dissolution. In BSE photomicrographs, subhedral-to-anhedral dark grey (low mean atomic number) crystal portions are surrounded by light grey (high mean atomic number) mantles + rims (Figs. 2 and 3). The innermost parts of resorbed cores are unaffected by dissolution features, showing compositions identical to those of the homogeneous cores. Accordingly, resorbed cores represent early-formed cognate clinopyroxenes that crystallized in equilibrium with the resident magma before partial dissolution and recrystallization caused by injections of hotter recharge melts;
- Type 3: recharge bands. Dark grey concentric growth zones developed within the clinopyroxene light grey mantle (Figs. 2 and 3). These recharge bands show sharp interfaces and are composed of continuous, planar segments, each of which responds to growth under a

certain crystal face. Within any given concentrically zoned overgrowth, the BSE intensity changes across the growth crystal boundary in the same sense, denoting that recharge bands are time-equivalent growth surfaces forming by supply of new magma to the advancing crystalline layer (Fig. 2 and 3). The darker BSE intensity of clinopyroxene cores, resorbed cores, and recharge bands is ascribed to higher contents of MgO and Cr_2O_3 and lower contents of Al_2O_3 and FeO compared to phenocryst mantles + rims (Fig. 3). Phenocrysts with recharge bands are more common in trachyte and rhyolite samples than in other rock types (Table 1);

- Type 4: mottled phenocrysts. Aggregation and/or conjoining of mutually touching resorbed crystals (Fig. 2), with indistinct boundaries due to the effect of dissolution (Dunworth et al., 2001). Mottled crystals are found from shoshonitic-to-rhyolitic products and their frequency increases with increasing degree of melt differentiation (Table 1). Irregular crystal portions show contrasting compositions, with both dark grey and light grey domains that are similar to those of resorbed cores and testify to dissolution and recrystallization of crystal aggregates during magma mixing;
- Type 5: sector-zoned phenocrysts. Sector zoning in clinopyroxene consists of hourglass (or basal) forms {-1 1 1} and prism forms {*h k* 0}, including {1 0 0}, {1 1 0}, and {0 1 0} faces. Sectors are identified by changes in BSE intensity from darker hourglass to lighter prism (Fig. 2) and are found only in shoshonites and latites (Table 1). Hourglass sectors grow faster along the c-axis, whereas prism sectors grow slower perpendicular to the *c* crystallographic axis (e.g., Ubide et al., 2020 and references therein). A growth sector boundary marks the interface between adjacent {-1 1 1} and {*h k* 0} forms, showing shapes either straight or slightly curved due to local variations in growth rates on the two faces (Fig. 2). Hourglass sectors are enriched in SiO_2 + MgO and depleted in Al_2O_3 + FeO_{tot} compared to prism sectors (Fig. 3). Both these sectors are sometimes crossed by concentric banding with sharp interfaces subparallel to the growing sector boundary (Fig. 2).

4.2. Clinopyroxene major elements

The whole data set derived for clinopyroxene major and trace element analyses is reported in Supplementary Material 1, together with variation diagrams where all the compositions of clinopyroxene cores, mantles + rims, and recharge bands are displayed on single plots.

Using the classification scheme reported in the review of Mollo et al. (2020b), we have calculated clinopyroxene cation fractions (X) and components (i.e., diopside, Di, $CaMgSi_2O_6$; hedenbergite, Hd, $CaFeSi_2O_6$; enstatite, En, $Mg_2Si_2O_6$; ferrosilite, Fs, $Fe_2Si_2O_6$), for each crystal population. Clinopyroxene cores are classified as diopside to diopside-augite (Di_{66-83}-Hd_{9-19}-En_{7-11}-Fs_{1-3}), whereas recharge bands and mantles + rims can be classified as augite (Di_{64-73}-Hd_{13-20}-En_{11-12}-Fs_{2-4} and Di_{65-61}-Hd_{19-21}-En_{13-16}-Fs_{4-5}, respectively).

Fig. 4 shows the Mg-number [Mg# = X_{Mg} / (X_{Mg} + X_{Fe2+}), where X is the cation fraction and all iron is expressed as Fe^{2+}] of clinopyroxene plotted against the sum of Di + Hd components (i.e., ΣDiHd) and the concentration of TiO_2 in phenocryst cores and phenocryst mantles + rims compared with recharge bands. The most relevant crystal chemical changes are presented here as average compositions of single samples. This comparison highlights that ΣDiHd decreases from clinopyroxene cores + recharge bands (0.80-0.88 on average) to clinopyroxene mantles + rims (0.76-0.79 on average). Conversely, the concentration of TiO_2 increases from 0.2 to 0.6 wt.% on average, as the growth of clinopyroxene takes place in more differentiated melt compositions (Fig. 4).

The Mg# of phenocryst cores abruptly decreases from basalts ($Mg\#_{91}$ on average) to shoshonites + latites ($Mg\#_{84-85}$ on average) to trachytes ($Mg\#_{82}$ on average) to rhyolites ($Mg\#_{78}$ on average), resembling the geochemical evolution of the host rocks (compare Figs. 1 and 4). Importantly, clinopyroxene is an early liquidus phase and its core is in equilibrium with the bulk rock composition as previously determined by Palummo et al. (2020). The equilibrium condition between clinopyroxene core and bulk rock compositions has been tested by the Fe-Mg exchange

(0.28 ± 0.08) of Putirka (2008), in conjunction with models based on the difference (Δ) between measured vs. predicted ΣDiHd components (Mollo et al., 2013; Mollo and Masotta, 2014) and thermodynamically-predicted partition coefficients for Na (Blundy et al., 1995) and Ti (Mollo et al., 2018, 2020). Due to the effects of magma mixing and hybridization phenomena, the equilibrium partitioning of Fe, Mg, Ti, and Na cations between the early-formed core and host magma has been restored by adding/subtracting to the bulk rock minimum amounts of minerals along the olivine-clinopyroxene-plagioclase cotectic (see supplementary data in Appendix A of Palummo et al., 2020). ΣDiHd decreases with proceeding magma differentiation from basalts (0.88 ± 0.01 on average) to latites + shoshonites + less differentiated trachytes (0.83 ± 0.01 on average) to more differentiated trachytes + rhyolites (0.80-0.82 ± 0.01 on average). The amount of TiO_2 in clinopyroxene remains almost identical from shoshonite to rhyolite (0.3-0.4 wt.% ± 0.04 on average). Conversely, diopsidic phenocrysts from mantle-derived basaltic rocks are characterized by lower TiO_2 concentrations (0.2 ± 0.04 wt.% on average; Fig. 4).

The entire compositional range of recharge bands is between $Mg\#_{80}$ and $Mg\#_{88}$, with an average of $Mg\#_{82}$ (Fig. 4). Recharge bands are more differentiated than diopsidic cores found in mantle-derived basalts and mimic the chemistry of clinopyroxene cores from shoshonites, latites, and trachytes. This compositional feature supports the idea of a polybaric-polythermal magmatic differentiation within the crust that proceeds in cooperation with recurrent mixing and hybridization processes (Gioncada et al., 2003). A small population of recharge bands from rhyolites (~13% of the whole data set) exhibits low TiO_2 abundances (≤0.2 wt.%; Fig. 4) resulting from the increased stability of titanomagnetite in the upper crust (Palummo et al., 2020).

Clinopyroxene mantles + rims from basalts to rhyolites depict a narrower and more evolved compositional range of $Mg\#_{75\text{-}78}$ relative to phenocryst cores + recharge bands (Fig. 4). The amount of ΣDiHd significantly decreases in clinopyroxene mantles + rims, especially due to strong CaO depletion caused by the incipient late-stage crystallization of feldspar (plagioclase + sanidine) during magma cooling and decompression (De Astis et al., 2013). Clinopyroxene mantles + rims from basalts (Mg#$_{78}$ on average) remain systematically less differentiated than those (Mg#$_{76}$ on average) from other rocks. Most of the compositions of mantles + rims from shoshonites to rhyolites overlap, without displaying any clear evolutionary trend neither for ΣDiHd or TiO_2 (Fig. 4). Clinopyroxene mantles + rims from latites (Mg#$_{75}$ on average) are slightly more evolved than those from rhyolites (Mg#$_{76}$ on average), in agreement with the increased number of recharge bands observed in phenocrysts from silicic host rocks and suggesting recurrent inputs of fresh and more primitive magmas from depth (Table 1).

4.3. Clinopyroxene trace elements

The chondrite-normalized patterns (Sun and McDonough, 1989) of rare earth elements (REE) in clinopyroxenes exhibit sub-parallel trends, shifting towards progressive trace element enrichments from basalt to rhyolite according to the more differentiated character of magma (Fig. 5). The concentration of light REE (LREE) is typically higher than that of heavy REE (HREE). Clinopyroxene mantles + rims exhibit lower LREE/HREE ratios (i.e., the normalized La/Yb ratio; La_N/Yb_N) and more pronounced negative Eu anomalies (i.e., $Eu/Eu^* = Eu_N/(Sm_N \times Gd_N)^{0.5}$) than clinopyroxene cores and recharge bands (Fig. 5). From basalts to rhyolites, both Eu/Eu* and La_N/Yb_N measured in clinopyroxene cores decrease from ~0.92 ± 0.06 to ~0.61 ± 0.06 on average and from ~2.8 ± 0.2 to ~2.3 ± 0.2 on average, respectively. In clinopyroxene mantles + rims, the values of Eu/Eu* and La_N/Yb_N further decrease to ~0.5 and ~2.0, respectively, responding to the abundant crystallization of feldspar at the late stage of melt differentiation.

The primordial mantle-normalized patterns (Sun and McDonough, 1989) of trace elements in clinopyroxenes show typical features of arc magmas, with enrichments in large ion lithophile element (LILE) to high field strength element (HFSE) ratios (Fig. 5). Both clinopyroxene cores, recharge bands, and mantles + rims display troughs at Ba, K, Nb, P, Zr, and Ti in (Fig. 5). The concentration of incompatible elements in clinopyroxene cores shows a marked increase from basalts to rhyolites, while the incompatible element concentrations partly overlap in clinopyroxene mantles + rims from trachytes to rhyolites (Fig. 5). Negative spikes of K, Sr, P, and Ti are more marked in clinopyroxene cores from trachytes and rhyolites, in agreement with the phase assemblage (i.e., feldspar + oxide ± apatite) that characterizes the more differentiated eruptions.

From clinopyroxene cores to recharge bands to mantles + rims, the amount of compatible transition elements (TE) decreases from 1,005 to 242 ppm and from 99 to 89 ppm for Cr and Ni, respectively. In particular, Cr is extremely high in phenocrysts from basalts (2,131 ± 102 ppm on average) relative to those from rhyolites (440 ± 107 ppm on average) and is well correlated with the Mg# of clinopyroxene. Conversely, V, Co, and Zn behave like incompatible elements and their average concentration increases with the host rock differentiation from 126 to 209 ppm, from 41 to 54 ppm, and from 40 to 76 ppm, respectively (Supplementary Material 1).

Scandium is highly compatible in clinopyroxene (cf. Mollo et al., 2020a) and its concentration decreases from clinopyroxene cores (87 ± 4 ppm on average) to mantles + rims (76 ± 2 ppm on average), resembling the progressive melt depletion with proceeding crystallization (Supplementary Material 1).

5. Discussion

5.1. The geochemical evolution of clinopyroxene

Fig. 6 shows that the differentiation path of magmas is faithfully recorded by major and trace element contents of clinopyroxene cores from products with different degrees of evolution. Diopsidic cores ($Mg\#_{91}$) from mantle-derived basalts support the idea of a unique deep level of magma, whose bulk composition is characterized by low incompatible LREE (i.e., Ce) and HFSE (i.e., Zr) concentrations, in conjunction with high TE/HREE ratios (i.e., Cr/Yb and V/Yb ratios; Fig. 6). Forsteritic ($Fo_{87–91}$) olivines are in equilibrium with diopsidic cores and the homogenization temperature of olivine-hosted melt inclusions indicates crystallization at T ≈ 1,190–1,250 °C (Gioncada et al., 1998). Thermobarometric constraints and thermodynamic calculations based on the equilibrium between clinopyroxene core and bulk rock compositions (see above), confirm that diopsidic phenocrysts equilibrated with primitive basaltic magmas at P_{max} ≈ 750 MPa and T_{max} ≈ 1,220 °C (Fig. 7). Primitive basaltic magmas are inferred to originate at mantle depths via partial melting of a depleted peridotitic source veined by metasomatic, clinopyroxene-rich regions (Kamenetsky and Clocchiatti, 1996). The occurrence of a mafic mineral assemblage in equilibrium with deep-seated magmas is in accordance with a Moho depth estimated at ~21–25 km, corresponding to *P* ≈ 620–740 MPa for a continental crust density of 2.7 g/cm^3 (Peccerillo et al., 2006 and references therein).

The *P*-*T* array traced by the crystallization of clinopyroxene changes significantly as the basaltic magmas migrate and differentiate towards two shallower and colder storage regions hosting 1) shoshonitic, latitic, and less differentiated trachytic melts at *P* ≈ 100-450 MPa and *T* ≈ 1,100-1,180 °C and 2) highly differentiated trachytic and rhyolitic melts at *P* ≤ 50 MPa and *T* ≤ 1,100 °C (Fig. 7). As *P* decreases, the stability field of clinopyroxene decreases in favor of olivine crystallization (Palummo et al., 2020) and the clinopyroxene composition shifts from diopside-augite ($Mg\#_{84\text{-}85}$) to augite ($Mg\#_{82\text{-}77}$). More evolved magmas residing at shallower crustal conditions are saturated with feldspar and titanomagnetite at *T* < 1,100 °C (Fig. 7). The abundant formation of plagioclase is also promoted by cooling-decompression regimes related to H_2O exsolution and degassing (cf. Mandarano et al., 2016 and references therein). Ce and Zr enrichments in clinopyroxene cores from basalts to rhyolites are in accord with the progressive differentiation of magma (Fig. 6). The Mg# of clinopyroxene plotted against the TE/HREE ratio highlights that basalts, shoshonites + latites, and trachytes + rhyolites cluster at different degrees of evolution (Fig. 6). In particular, the abrupt decrease of Cr/Yb ratio from basalts (9,500-12,500) to shoshonites + latites (500-2,500) to trachytes + rhyolites (100-500; Fig. 6) confirms the early and extensive crystallization of mafic minerals (olivine + clinopyroxene), in which Cr is prevalently incorporated (e.g., Tecchiato et al., 2018). As the composition of magma evolves, the concentration of incompatible Ce and Zr elements progressively increases in clinopyroxene cores. At the same time, the increasing stability of plagioclase leads to stronger negative Eu anomalies (Eu/Eu*) and lower LILE/HREE ratios (i.e., Sr/Yb ratios), especially for trachytes and rhyolites (Fig. 6). Silicic magmas are stored in upper and colder crustal environments located at $P \leq 50$ MPa (Fig. 7) and, likely, are generated by the extraction of interstitial melts from crystal-rich (mushy) reservoirs. Abundant segregation of feldspar phenocrysts is inferred to be responsible for the development of distinct magma-mush pockets (Palummo et al., 2020; Nicotra et al., 2018). Feldspar-liquid separation processes can be also favored by second boiling of the melt and consequent volatile exsolution of a fluid phase at $T \approx 860$–1,100 °C and H_2O concentrations in excess of ~2.5–4.0 wt.% (Gioncada et al., 2003; Costa et al., 2020; Palummo et al., 2020).

Intracrystalline heterogeneities in clinopyroxene are recorders of recurrent magma recharge and mixing events (Type 3 recharge bands; Figs. 2 and 3), generally accompanied by multi-stage crystal dissolution phenomena (Type 2 resorbed cores and Type 4 mottled aggregates; Figs. 2 and 3). Resorbed cores are interpreted as evidence of corrosion by thermal and/or chemical disequilibrium with the melt. This open-system behavior is caused by the injection of hotter and more mafic magmas into compositionally distinct reservoirs within the crust (Bullock et al., 2019; Costa et al., 2020; De Astis et al., 2013; Nicotra et al., 2018). Concentric Cr zonation in clinopyroxene indicates subtle modulations in the history of melt composition involved in clinopyroxene growth (Fig. 3). Several clinopyroxene phenocrysts contain Cr-rich resorbed cores that likely formed by replenishment of the crystallizing reservoir. These cores were partially dissolved during protracted storage at magmatic temperature and finally incorporated into the new recharge melt (Ubide and Kamber, 2018; Mollo et al., 2020a). Owing to the broad compositional range of clinopyroxene-bearing magmas (Fig. 1a), the destabilization-dissolution of clinopyroxene cores is probably controlled by mutual thermal and chemical effects caused by the transport of crystals through the upper crust (e.g., Mollo and Masotta, 2014; Forni et al., 2016, 2018). In a similar fashion, the formation of Type 3 concentrically zoned phenocrysts can be ascribed to repeated recharge events that are inferred to be drivers of convective dynamics in crustal storage regions (Bergantz et al., 2015). Given that some Cr-rich bands developed at the clinopyroxene rim (Fig. 3), it is plausible that the eruption was triggered by the injection of mafic magma (Ubide and Kamber, 2018; Petrone et al., 2018). Magma mixing is frequently suggested as an effective eruption trigger (Sparks et al., 1977; Druitt et al., 2012) and is sometimes associated with volatile exsolution during magma ascent from depth towards the surface (Cashman et al., 2017).

Fig. 8 shows that recharge bands ($Mg\#_{81\text{-}85}$) are markers of primitive REE-HFSE-poor, TE-rich magmas injecting into more differentiated REE-HFSE-rich, TE-poor domains, where clinopyroxene mantles + rims ($Mg\#_{75\text{-}78}$) developed at the late stage of magma mixing-hybridization. The abrupt decrease of averaged Sr/Yb ratio from 89 (recharge bands) to 42 (mantles + rims) and the strong negative Eu anomaly (Fig. 8) confirm that most of the evolutionary path is controlled by incipient plagioclase crystallization (De Astis et al., 2013; Nicotra et al., 2018). In view of this magma compositional shift, the concentration of Zr markedly increases up to 52 ppm in clinopyroxene mantles + rims, whereas the Cr/Yb ratio reaches a minimum of 0.5 (Fig. 8). It is also interesting to note that clinopyroxene mantles + rims from trachytes and rhyolites appear less differentiated than expected for silicic magmas, mostly showing major and trace element contents similar to the crystal cargo of basaltic and shoshonitic products (Fig. 8). This compositional observation matches with the numerous recharge bands enclosed within clinopyroxenes from trachytes and rhyolites (Table 1), attesting to continuous replenishment of the shallow plumbing system and consequent magma hybridization within the crystal mush (e.g., Forni et al., 2016).

Type 5 sector-zoned clinopyroxene phenocrysts are sporadically found in shoshonites and latites (Figs. 2 and 3). Si-Mg-rich hourglass forms {-1 1 1} are depleted in REE (e.g., Ce = 14 ± 1.2 and Yb = 1 ± 0.01 ppm on average) and HFSE (e.g., Hf = 1 ± 0.01 ppm and Zr = 19 ± 1.3 ppm on average) relative to Al-Fe-rich prism forms {*h k* 0} (e.g., Ce = 31 ± 3.1 ppm, Yb = 3 ± 0.02 ppm, Zr = 36 ± 3.4 ppm, and Hf = 2 ± 0.02 ppm on average). The intracrystalline distribution of major cations among the different sectors agrees with that observed for sector-zoned augites at Mt. Etna (Downes, 1974; Ubide et al., 2019a) and Stromboli (Ubide el al., 2019b). Sectoral partitioning of

REE and HFSE cations is strictly controlled by both charge-balanced and -imbalanced configurations taking place in the structural sites of {-1 1 1} and {*h k* 0} sectors as the number of Al cations in tetrahedral coordination increases (Ubide et al., 2019a). The magnitude of sectoral partitioning at Vulcano Island is very similar to that measured at Stromboli, whereas the compositional difference between {-1 1 1} and {*h k* 0} sectors is much more marked for the clinopyroxene populations at Mt. Etna. For example, the $Al_2O_{3\{-1\ 1\ 1\}}/Al_2O_{3\{h\ k\ 0\}}$ ratios in phenocrysts at Vulcano Island, Stromboli, and Mt. Etna are on the order of 0.88, 0.81, and 0.58, respectively. According to literature, the differential partitioning of cations between {-1 1 1} and {*h k* 0} faces is proportional to the degree of undercooling that, in turn, governs the growth of clinopyroxene under different magmatic conditions (Kouchi et al. 1983; Welsch et al., 2016; Ubide el al., 2019b; Giuliani et al., 2020; Masotta et al., 2020). Ubide el al. (2019b) compared the stronger sector zonation of clinopyroxenes from Mt. Etna with the weaker sector zonation of crystals from Stromboli. The authors concluded that the slow growth of clinopyroxene at Stromboli was generated by magmas undergoing very low degrees of undercooling comprised between 10 and 20 °C. Building on constraints from clinopyroxene growth experiments carried out by Kouchi et al. (1983), we observe that $Al_2O_{3\{-1\ 1\ 1\}}/Al_2O_{3\{h\ k\ 0\}}$ ratios for phenocrysts from Vulcano Island and Stromboli are generated by a degree of undercooling of ~13 °C. On the other hand, Masotta et al. (2020) have experimentally documented that sectoral partitioning of natural phenocrysts from Mt. Etna is caused by higher degrees of undercooling, mostly comprised between 23 and 32 °C. In this regard, magma dynamics driving the eruption of shoshonites-latites at Vulcano Island can be interpreted as the effect of sluggish crystallization kinetics under growth-dominated regimes during very slow magma ascents (Ubide el al., 2019b). It is also plausible that sector-zoned clinopyroxenes originated by small-scale convective transport of crystals through thermally heterogeneous magma reservoirs (cf. Welsch et al., 2009) that are located within the plumbing system at ~10-17 km of depth (De Astis et al., 2013; Palummo et al., 2020).

5.2. Timescales record of pre-eruptive processes

As discussed above, high-Mg# and Cr_2O_3-rich recharge bands of Type 3 clinopyroxene phenocrysts (Figs. 2 and 3) indicate crystallization from 1) a high-*T*, mafic magma that is recorded by the recharge band and 2) a low-*T*, resident magma which is homogenized by mixing and hybridization after the mafic injection. Fe-Mg compositional zoning profiles in clinopyroxene phenocrysts have been examined to quantify the crystal residence time (Δt) via elemental diffusion chronometry using the NIDIS (Non-Isothermal Diffusion Incremental Step) model of Petrone et al. (2016). BSE microphotographs and greyscale profiles are used as proxies for Fe-Mg compositional zoning boundary layers along transects normal to the recharge band-rim interface (see Supplementary Material 2). The crystallization temperatures of clinopyroxene recharge bands and rims in equilibrium with different melt components have been calculated by using thermobarometric models based on exchange equilibria (cf. Palummo et al., 2020; see also temperature histograms in Supplementary Material 1): 1) 1,200-1,220 °C (high-Mg# recharge band) and 1,190-1,200 °C (low-Mg# rim) for basalts, 2) 1,130-1,180 °C (high-Mg# recharge band) and 1,100-1,160 °C (low-Mg# rim) for shoshonites, latites, and trachytes, and 3) 1,090-1,100 °C (high-Mg# recharge band) and 1,080-1,090 °C (low-Mg# rim) for rhyolites. The error of estimate has been minimized by probability density function analysis and corresponds to ±15 °C. We adapted the NIDIS model to evaluate the diffusive timescale (Δt) in the low-*T* resident magma (i.e., recharge band-rim interface) which represents the time spent in the last magmatic environment prior to eruption (Petrone et al., 2016).

Smoother recharge band-rim profiles are generally observed in clinopyroxenes from silicic rocks, in agreement with longer temporal intervals after mafic injection in the reservoir and prior to eruption (Fig. 9a). Conversely, steeper diffusion profiles are measured for recharge band-rim boundaries analyzed in clinopyroxene phenocrysts from more primitive products, as the result of diffusive re-equilibration of compositional zoning for shorter time periods (Fig. 9a). All timescales are summarized in Fig. 9b. Shorter timescales of ∼0.1-9 years are quantified for clinopyroxenes from basalts, shoshonites, and latites, whereas longer timescales on the order of ~7-18 years and ~16-44 years are calculated for clinopyroxenes from trachytes and rhyolites, respectively (Fig. 9b). The longer crystal residence times measured for the more differentiated eruptive products are in agreement with the general increase over time of the degree of chemical evolution of magmas and the enrichment in incompatible trace elements (e.g., De Astis et al., 2013). This time-related compositional shift from basalts to rhyolites is also confirmed by the geochemical evolution of clinopyroxene core from Eruptive Epoch 5 to 8 (Fig. 6).

Mixing phenomena between high-T mafic and low-T felsic end-members are intimately related to magma dynamics recorded by the recurrent concentric zonation and dissolution texture of clinopyroxene phenocrysts, which tend to be slightly more abundant in trachyte and rhyolite (Figs. 2 and 3; Table 1). More silicic trachytes and rhyolites represent residual melts trapped-extracted from crystal mushes that are approximatively located between 5 and 10 km depth (Palummo et al., 2020). The most favorable window for crystal-melt separation occurs at a crystallinity of ~50–70% (Dufek and Bachmann, 2010), such that eruptible silicic melts can be extracted from the crystal mush, without bulk melting or remobilization of its crystalline framework (Stelten et al., 2015). Coherently, the differentiation of basalts to trachytes at Vulcano Island takes place at crystal content of ~52%, whereas the formation of highly differentiated trachytes and rhyolitic melts requires a mush system with crystallinity comprised between 59% and 84% (Palummo et al., 2020).

The compositional similarity between clinopyroxene cores and mantles + rims from trachytes and rhyolites (compare Figs. 6 and 8) suggests mutual crystallization in a colder and shallower mush region over prolonged crystal residence times (Fig. 9). The great number of recharge bands observed in silicic products, alongside resorbed cores and mottled crystals (Table 1) indicates that phenocrysts remained trapped in the mush for a prolonged period of time, thereby recording sustained injections of less differentiated magmas. Longer diffusion timescales are typically measured for phenocrysts hosted in silicic melts extracted from crystal-rich regions (Cooper, 2019). By interpolating 1) the empirical viscosity equation of Giordano et al. (2008), 2) the bulk rock analyses of products erupted at Vulcano Island (Fig. 1a), and 3) the *P*-*T*-H_2O crystallization paths of clinopyroxene-bearing magmas (Palummo et al., 2020), we found that the geochemical evolution of clinopyroxene is accompanied by an average melt viscosity increase, on the order of ~1.2 (basalt), ~2.3 (shoshonite), ~2.5 (latite), ~3.8 (trachyte), ~4.6 (rhyolite) log Pa s. In the lower crust, low viscosity basaltic magmas remain above the solidus state due to the effect of high temperature conditions. These thermal and rheological regimes allow extensive magma segregation and migration. During ascent, however, basaltic magmas cool and crystallize to develop more differentiated melts leading to the growth of clinopyroxene phenocrysts progressively more enriched in REE and HFSE (Figs. 5 and 6). In the uppermost crust, the formation of non-eruptible crystal-rich mush regions takes place by strong cooling-induced crystallization phenomena and high viscosity rhyolitic lenses develop by percolative melt transfer (Bachmann and Bergantz, 2004; Dufek and Bachmann, 2010; Masotta et al., 2016). Protracted residence times recorded by clinopyroxene phenocrysts (Fig. 9) are consistent with the tendency for phenocrysts to remain suspended in more silicic melts with a higher viscosity, as the temperature of the solidifying system decreases and the degree of crystallization increases (e.g., Hawkesworth et al., 2000 and references therein). As outlined by thermobarometric constraints (Fig. 7), after extraction of melt from the crystal mush, small-volume rhyolitic magmas stall temporarily at very shallower levels of the reservoir. Therefore, resorbed cores (Type 2), recharge bands (Type 3), and mottled resorption textures (Type 4) found in clinopyroxene phenocrysts (Figs. 2 and 3) may be also interpreted as the result of mixing between low-*T* rhyolitic magmas extracted from the crystal-rich region and fresh inputs of high-*T* free magmas rising from shoshonitic and latitic reservoirs located at moderate depths of 10-17 km (De Astis et al., 2013; Palummo et al., 2020).

5.3. Modeling magma recharge and mixing dynamics

Cr/Yb ratios measured for clinopyroxene cores, recharge bands, and mantles + rims are comparatively plotted in Fig. 10a in order to place constrain on the recharge processes and mixing dynamics governing the evolutionary history of magmas at Vulcano Island. An important aspect emerging from this comparison is the compositional diversity of clinopyroxene, characterized by decreasing Cr/Yb ratios as the geochemical evolution of magma proceeds from basalt to rhyolite (Fig. 10a). Differently from the more homogeneous chemistry of basalts erupted during the Eruptive Epoch 5, younger rhyolitic melts from Eruptive Epoch 8 were dominated by abundant crystallization of felsic minerals plus low degrees of crustal assimilation (Bullock et al., 2019; De Astis et al., 1997, 2000, 2003; Gioncada et at., 2003; Peccerillo et al., 2006). Clinopyroxene zoning patterns with highly variable Cr/Yb ratios reflect substantial chemical modifications in more silicic reservoirs due to open-system processes associated with the input of fresh magma into distinct crustal regions and related mixing and hybridization phenomena (Forni et al., 2016; Gioncada et al., 1998; Nicotra et al., 2018; Peccerillo et al., 2006; Piochi et al., 2009). Moreover, Cr/Yb ratios in clinopyroxene decrease with the sequential growth of phenocryst, from core to mantle + rim (Fig. 10a). This change validates the idea that magma mixing was likely accompanied by cooling-degassing processes, especially during the storage of magma in shallower and colder crustal regions (Mandarano et al., 2016), where the most evolved chemistry of clinopyroxene rims reflects the latest residual melt composition, immediately preceding the eruption.

With the only exception represented by the diopsidic clinopyroxene cores from basalts, there is always some degree of overlap between the trace element inventory of clinopyroxene cores, recharge bands, and mantle + rims (Fig. 10a). As schematically illustrated in Fig. 10b, the compositional heterogeneity of clinopyroxene results from the transfer of magma between different storage regions that are interconnected with each other (cf. Palummo et al., 2020). The isolated compositional group of clinopyroxene cores from basalts with extremely high Cr/Yb ratios (Fig. 10a) represent early crystal-melt equilibration in the lower crust (Fig. 10b). Conversely, the Cr/Yb ratio in clinopyroxene cores from shoshonites to rhyolites progressively decreases (Fig. 10a), in accord with the formation of more differentiated reservoirs that, however, explore continuous physico-chemical changes due to interaction between compositionally distinct magma batches (Fig. 10b).

Recharge bands in clinopyroxene phenocrysts from basalts show Cr/Yb ratios that are intermediate between those measured for clinopyroxene cores from shoshonites + latites and trachytes + rhyolites (Fig. 10a). This suggests that an early-formed crystal cargo residing in the deeper parts of the crust was remobilized and transported by mafic melts (e.g., Petrone et al., 2018; Cooper, 2019) passing through an interconnected series of differentiated magma storage regions (Fig. 10b). In a similar fashion, the occurrence of Type 4 mottled phenocrysts (i.e., aggregates of partially dissolved clinopyroxenes; Fig, 2) suggests that crystals were assembled from different parts of the crust (Fig. 10b), in agreement with analogous dynamic processes documented for clinopyroxenes erupted at Mt. Etna (Armienti et al., 2007) and Stromboli (Di Stefano et al., 2020). In this scenario, intracrystalline heterogeneities indicate a multi-stage history of magma that is characterized by mixing and hybridization phenomena operating within an articulated plumbing system (Fig. 10b), where recharge inputs encounter partially or wholly crystallized reservoirs generated by different prior magma batches. The broad compositional interval recorded by recharge bands from rhyolites (Fig. 10a) testifies to multiple inputs of mafic magma from depth, abundant cooling-induced crystallization, and protracted crystal residence times in a highly crystalline storage region.

The bulk (crystal + melt) chemical evolution of magmas points towards a unified view of cogenetic differentiation processes operating in two main magma storage regions within the crust (cf. Bachmann and Huber, 2016). The first storage region is located in lower crust near the crust-mantle boundary and is fed by primitive basalts that represent the most mafic endmembers of the differentiation series (Fig. 10b). A high-pressure crystallization assemblage develops within this lower crustal storage region (see for example Ozdemir et al., 2011). The second main storage region is located at shallower depths in the upper crust (typically between 250 and 150 MPa; see Huber et al., 2019), where magmas pond at the apex of a series of interconnected magma transfer zones (Fig.

10b). Magma dynamics at Vulcano Island are controlled by the interplay between lower and upper crust storage regions and only transient magma bodies are generated at intermediate depths (Fig. 10b), partly by mixing of magmas from these two main storage regions (Bachmann and Huber, 2016; Huber et al., 2019).

To better elucidate the clinopyroxene-related geochemical changes characterizing the eruptive history of Vulcano Island, we have investigated the evolutionary path of LREE (i.e., La) and HREE (i.e., Yb) in magmas through the partitioning model of Mollo et al. (2018, 2020b). Different equations describing the excess of strain energy (Wood and Blundy, 1997) and electrostatic energy (Wood and Blundy, 2001) are integrated in this model, in order to calculate the partitioning energetics controlling heterovalent REE cation substitutions in clinopyroxene. This makes it possible to quantify the role of clinopyroxene crystallization on the REE pattern of a magma through the estimate of a different clinopyroxene-melt partition coefficient (i.e., $D_{REE} = {}^{cpx}REE / {}^{melt}REE$ on a weight basis) for each stage of crystallization. The *P*-*T*-H_2O saturation conditions of clinopyroxene phenocrysts (i.e., *P* = 20-750 MPa, *T* = 1,000-1,220 °C, and H_2O = 1.6-4.0 wt.%) that are required as input data for the partitioning modeling come from the petrological work of Palummo et al. (2020). REE cations were chosen for the modeling because of 1) the diverse but systematic zoning patterns in clinopyroxene phenocrysts, 2) the complete thermodynamic description of partitioning behavior as a function of intensive-extensive parameters, and 3) the preferential control of clinopyroxene crystallization on REE contents in the residual melt relative to other mineral phases (i.e., according to the relation between mineral weight fractions and the bulk partition coefficient; Mollo et al., 2018, 2020b). A spectrum of partition coefficients has been determined for clinopyroxene cores and recharge bands (Supplementary Material 1). Recalling the free energy exchange of the fusion reaction ${}^{cpx}REEMgSiO_2O_6 \leftrightarrow {}^{melt}REEMgSiO_2O_6$ (Wood and Blundy, 1997), the estimated values of D_{La} and D_{Yb} were used to invert the concentrations of REE in the melts from clinopyroxene cores and recharge bands (i.e., ${}^{melt}REE = {}^{cpx}REE / D_{REE}$).

Results from calculations are plotted in Fig. 10c and compared with the bulk rock analyses of the eruptive products. Different compositional vectors (i.e., colored arrows in Fig. 10c) represent the putative REE contents of end-member magmas in equilibrium with the more homogeneous clinopyroxene cores, as calculated by the partitioning equations of Mollo et al. (2018, 2020b). These vectors are almost aligned along a common differentiation path involving the progressive increase of La-Yb contents from basalt to rhyolite. The La-Yb array resulting from partitioning modeling is divided in three distinct groups for basalts, shoshonites + latites, and trachytes + rhyolites (Fig. 10c) that roughly reflect the plumbing system architecture of Vulcano Island (Fig. 10b). The grey dashed symbols represent the putative REE contents of magmatic injections recorded by the more heterogeneous recharge bands (Fig. 10c). While most of recharge bands from basalts converge in a narrow range that is close to the compositional vector, recharge bands from trachytes and rhyolites show the largest compositional variability. This implies that the number of recharge bands and their chemical diversity axiomatically increase with increasing the silicic character of magma, thereby depicting a fan-like array indicative of open-system processes (Fig. 10c). Importantly, our modelled data set reproduce very well the bulk rock analyses of natural eruptions and their fan-like pattern (Fig. 10c). This correspondence reflects a plumbing system evolution that is persistently controlled by crystal-melt dynamics due to the interaction between different crystallizing reservoirs in which the supply of fresh magma modulates the final texture and composition of the erupted product.

We conclude that the lower crust is the most favorable location for the origin of compositionally homogeneous basaltic magmas (i.e., melt-dominated domains) and their initial stages of crystallization during transfer at intermediate depths (Fig. 10b). However, magma percolation and accumulation in the upper crustal regions lead to the formation of an interconnected series of magmatic reservoirs (i.e., crystal-dominated domains), many of which may be composed of crystal-rich mush systems (Fig. 10b). According to this conceptual model, the physical (e.g., crystallinity and melt viscosity) and chemical (e.g., degree of evolution of crystals and melts) state of magma changes dramatically in the shallowest parts of the feeding system. The discrete populations, complex compositional zoning patterns, and different residence times of clinopyroxene phenocrysts reflect the intricate crystallization history of magma. The mineral assemblage in silicic mush melts is sufficiently resilient to record numerous mafic injections and high degrees of magma mixing, hybridization, and crystallization before eruption. Taken together, the textural and compositional changes of clinopyroxene phenocrysts present a picture of a plumbing system that extends through the crust and is characterized by distributions of melts and crystals which are progressively more evolved and heterogeneous in both space and time (Fig. 10b).

6. Concluding remarks

This study illustrates the textural and compositional changes of clinopyroxene phenocrysts from basaltic to rhyolitic products erupted at Vulcano Island over a period of time from ~54 ka to 1739 CE. Phenocrysts have been categorized on the presence or absence of complex zoning patters and five distinct populations have been recognized (i.e., Type 1 homogeneous crystals, Type 2 core/resorbed cores, Type 3 recharge bands, Type 4 mottled crystals, and Type 5 sector-zoned crystals). The different growth features and intracrystalline distributions of major and trace cations in clinopyroxene closely reflect the physico-chemical changes of magma under the effects of closed- and open-system processes. By combining microanalytical data and trace element modeling, we gained useful insights into the plumbing system architecture and the intricate magmatic history of Vulcano Island. According to this approach, the following conclusions can be drawn:

1) the compositional evolution of clinopyroxene highlights that basaltic magmas are characterized by Types 1 and 2 populations, in which diopsidic cores are heralds of crystallization in the lower crust. The compositional change of clinopyroxene proceeds from diopside-augite to augite, following the polybaric-polythermal differentiation of basalts towards more differentiated melts residing in the upper crust;

2) the number of chemical heterogeneities in clinopyroxene increases in silicic eruptive products, in accord with the more frequent observation of Types 3 and 4 populations in trachytes and rhyolites. This chemical diversity reflects an open-system behavior due to injection of hotter and more primitive magmas into compositionally distinct colder and shallower reservoirs. Open-system processes are testified by multi-stage clinopyroxene dissolution phenomena that results from thermal and/or chemical disequilibrium with the recharge melt;
3) Type 5 sector-zoned crystals are typically found in shoshonites and latites. The weak sector zonation between {-1 1 1} hourglass and {*h k* 0} basal prism forms suggests sluggish crystallization kinetics during very slow magma ascents and/or small-scale convective transport of crystals through thermally heterogeneous magma reservoirs;
4) shorter timescales (~0.1-9 years) are quantified for clinopyroxenes from basaltic, shoshonitic, and latitic magmas, whereas longer timescales are measured for phenocrysts crystallizing in trachytic (~7-18 years) and rhyolitic (~16-44 years) reservoirs. Protracted residence times are consistent with the tendency for clinopyroxene to remain suspended in more silicic and viscous melts extracted from shallow crystal-rich regions;
5) results from partitioning modeling based on the concentrations of rare earth elements (REE) in clinopyroxene confirm the cogenetic origin for the eruptive products along a common differentiation path. Magma percolation and accumulation in the upper crustal regions lead to the formation of an interconnected series of magmatic reservoirs with different degrees of REE concentrations. Both the compositional diversity of melt and the intracrystalline heterogeneity of clinopyroxene are exacerbated in crystal-dominated mush zones, responding to the stronger diversification of REE via intense magma mixing, hybridization, and crystallization phenomena.

Acknowledgments

This work has been greatly improved by the helpful and thoughtful reviews of Andreas Klügel and one anonymous reviewer. Michael Roden is also acknowledged for his valuable editorial guidance.

References

Armienti, P., Francalanci, L., Landi, P., 2007. Textural effects of steady state behavior of the Stromboli feeding system. J. Volcanol. Geotherm. Res. 160, 86-98.

Bachmann, O., Huber, C., 2016. Silicic magma reservoirs in the Earth's crust: American Mineralogist, v. 101, p. 2377-2404.

Bachmann, O., Bergantz, G.W., 2004. On the origin of crystal-poor rhyolites: extracted from batholithic crystal mushes. J. Petrol. 45 (8), 1565-1582.

Beard, C.D., van Hinsberg, V.J., Stix, J., Wilke, M., 2019. Clinopyroxene/melt trace element partitioning in sodic alkaline magmas. J. Petrol. 60, 1797-1823. https://doi.org/10.1093/petrology/egz052.

Bergantz, G.W., Schleicher, J.M., Burgisser, A., 2015. Open-system dynamics and mixing in magma mushes. Nature Geoscience, 8(10), 793-796.

Blundy, J. D., Falloon, T. J., Wood, B. J., Dalton, J. A., 1995. Sodium partitioning between clinopyroxene and silicate melts. J. Geophys. Res. Solid Earth, 100, 15501-15515.

Bullock, L.A., Gertisser, R., O'Driscoll, B., Harland, S., 2019. Magmatic evolution and textural development of the 1739 CE Pietre Cotte lava flow, Vulcano, Italy. J. Volcanol. Geoth. Res. 372, 1-23.

Cashman, K.V., Sparks, R.S.J., Blundy, J.D., 2017. Vertically extensive and unstable crystals mushes: a unifying view of igneous processes associated with volcanoes. Science 355 (6331) eaag3055.

Clocchiatti, R., Del Moro, A., Gioncada, A., Joron, J.L., Mosbah, M., Pinarelli, L., Sbrana, A., 1994. Assessment of a shallow magmatic system: the 1888-90 eruption, Vulcano Island, Italy. Bull. Volcanol. 56, 466-486.

Cooper, K.M., 2019. Time scales and temperatures of crystal storage in magma reservoirs: Implications for magma reservoir dynamics. Philosophical Transactions of the Royal Society A, 377(2139), 20180009.

Costa, S., Masotta, M., Gioncada, A., Pistolesi, M., Bosch, D., Scarlato, P., 2020. Magma evolution at La Fossa volcano (Vulcano Island, Italy) in the last 1000 years: evidence from eruptive products and temperature gradient experiments. Contrib. Mineral. Petrol. 175 (4), 1-22.

Costa, S.; Masotta, M.; Gioncada, A.; Pistolesi, M. A Crystal Mush Perspective Explains Magma Variability at La Fossa Volcano (Vulcano, Italy). Minerals, 2021, 11, 1094. https://doi.org/10.3390/min11101094

Davì, M., De Rosa, R., Donato, P., Vetere, F., Barca, D., Cavallo, A., 2009. Magmatic evolution and plumbing system of ring-fault volcanism: the Vulcanello peninsula (Aeolian Islands, Italy). Eur. J. Mineral. 21, 1009-1028.

De Astis, G., La Volpe, L., Peccerillo, A., Civetta, L., 1997. Volcanological and petrological evolution of Vulcano Island (Aeolian Arc, southern Tyrrhenian Sea). J. Geophys. Res. 102, 8021-8050.

De Astis, G., Peccerillo, A., Kempton, P.D., La Volpe, L., Wu, T.W., 2000. Transition from calc-alkaline to potassium-rich magmatism in subduction environments: geochemical and Sr, Nd, Pb isotopic constraints from the island of Vulcano (Aeolian arc). Contrib. Mineral. Petrol. 139, 684-703.

De Astis, G., Ventura, G., Vilardo, G., 2003. Geodynamic significance of the Aeolian volcanism (Southern Tyrrhenian Sea, Italy) in light of structural, seismological, and geochemical data. Tectonics 22, 1040-1057.

De Astis, G., Lucchi, F., Dellino, P., La Volpe, L., Tranne, C.A., Frezzotti, M.L., Peccerillo, A., 2013. Geology, volcanic history and petrology of Vulcano (central Aeolian archipelago). In: Lucchi, F., Peccerillo, A., Keller, J., Tranne, C.A., Rossi, P.L. (Eds.), The Aeolian Islands Volcanoes. Geological Society, London, Memoirs vol. 37, 181-349.

Dellino, P., De Astis, G., La Volpe, L., Mele, D., Sulpizio, R., 2011. Quantitative hazard assessment of phreatomagmatic eruptions at Vulcano (Aeolian Islands, Southern Italy), as obtained by combining stratigraphy, event statistics and physical modelling. J. Volcanol. Geotherm. Res. 201, 364-384.

Di Stefano, F., Mollo, S., Ubide, T., Petrone, C. M., Caulfield, J., Scarlato, P., Nazzari, M., Andronico, D., Del Bello, E., 2020. Mush cannibalism and disruption recorded by clinopyroxene phenocrysts at Stromboli volcano: New insights from recent 2003–2017 activity. Lithos, 360, 105440.

Downes, M.J., 1974. Sector and oscillatory zoning in calcic augites from M. Etna, Sicily. Contrib. Mineral. Petrol. 47, 187-196.

Druitt, T.H., Costa, F., Deloule, E., Dungan, M., Scaillet, B., 2012. Decadal to monthly timescales of magma transfer and reservoir growth at a caldera volcano. Nature 482, 77-80.

Dufek, J., Bachmann, O., 2010. Quantum magmatism: Magmatic compositional gaps generated by melt-crystal dynamics. Geology 38 (8), 687-690.

Dunworth, E., Neumann, E.R., Rosenbaum, J., 2001. The Skien lavas, Oslo Rift: petrological disequilibrium and geochemical evolution. Contributions to Mineralogy and Petrology, 140(6), 701-719.

Ellam, R.M., Menzies, M.A., Hawkesworth, C.J., Leeman, W.P., Rosi, M., Serri, G., 1988. The transition from calc-alkaline to potassic orogenic magmatism in the Aeolian Islands, Southern Italy. Bulletin of Volcanology, 50, 386-398.

Forni, F., Ellis, B.S., Bachmann, O., Lucchi, F., Tranne, C.A., Agostini, S., Dallai, L., 2015. Erupted cumulate fragments in rhyolites from Lipari (Aeolian Islands). Contrib. Mineral. Petrol. 170, 49.

Forni, F., Bachmann, O., Mollo, S., De Astis, G., Gelman, S.E., Ellis, B.S., 2016. The origin of a zoned ignimbrite: Insights into the Campanian Ignimbrite magma chamber (Campi Flegrei, Italy), Earth and Planetary Science Letters, 449, 259-271. http://dx.doi.org/10.1016/j.epsl.2016.06.003.

Forni, F., Degruyter, W., Bachmann, O., De Astis, G., Mollo, S., 2018. Long-term magmatic evolution reveals the beginning of a new caldera cycle at Campi Flegrei. Science Advances 4 (11), eaat9401. http://dx.doi.org/10.1126/sciadv.aat9401.

Gioncada, A., Clocchiatti, R., Sbrana, A., Bottazzi, P., Massare, D., Ottolini, L., 1998. A study of melt inclusions at Vulcano (Aeolian Islands, Italy): insights on the primitive magmas and on the volcanic feeding system. Bull. Volcanol. 60, 286-306.

Gioncada, A., Mazzuoli, R., Bisson, M., Pareschi, M.T., 2003. Petrology of volcanic products younger than 42 ka on the Lipari-Vulcano complex (Aeolian Islands, Italy): an example of volcanism controlled by tectonics. J. Volcanol. Geotherm. Res. 122, 191-220.

Gioncada, A., Mazzuoli, R., Milton, A.J., 2005. Magma mixing at Lipari (Aeolian Islands, Italy): insights from textural and compositional features of phenocrysts. Journal of Volcanology and Geothermal Research, 145(1-2), 97-118.

Giordano, D., Russell, J.K., Dingwell, D.B., 2008. Viscosity of magmatic liquids: a model. Earth and Planetary Science Letters, 271(1-4), 123-134.

Giuliani, L., Iezzi, G., Mollo, S., 2020, Dynamics of volcanic systems: physical and chemical models applied to equilibrium versus disequilibrium solidification of magmas, p.101-132, in Vetere F. eds., Dynamic Magma Evolution, Geophysical Monograph Series 254, 206 pp., ISBN: 9781119521136, John Wiley & Sons Inc., New Jersey, USA. https://doi.org/10.1002/9781119521143.ch5.

Hawkesworth, C.J., Blake, S., Evans, P., Hughes, R., Macdonald, R., Thomas, L.E., Turner, S.P., Zellmer, G., 2000. Time scales of crystal fractionation in magma chambers-integrating physical, isotopic and geochemical perspectives. Journal of Petrology, 41(7), 991-1006.

Huber, C., Townsend, M., Degruyter, W., Bachmann O., 2019. Optimal depth of subvolcanic magma chamber growth controlled by volatiles and crust rheology. Nature Geoscience 12, 762–768.

Kamenetsky, V., Clocchiatti, R., 1996. Primitive magmatism of Mt. Etna: insights from mineralogy and melt inclusions. Earth Planet. Sci. Lett. 142 (3-4), 553-572.

Keller, J., 1980. The island of Vulcano. Rendiconti della Società Italiana di Mineralogia e Petrografia 3 (6), 369-414.

Kent, A.J.R., Darr, C., Koleszar, A. M., Salisbury, M.J., Cooper, K.M., 2010. Preferential eruption of andesitic magmas through recharge filtering. Nat. Geosci. 3, 631-636.

Kouchi, A., Sugawara, Y., Kashima, K., Sunagawa, I., 1983. Laboratory growth of sector zoned clinopyroxenes in the system CaMgSi2O6-CaTiAl2O6. Contributions to Mineralogy and Petrology, 83(1-2), 177-184.

Lanzafame, G., Mollo, S., Iezzi, G., Ferlito, C., Ventura, G., 2013. Unraveling the solidification path of a pahoehoe “cicirara” lava from Mount Etna volcano. Bulletin of Volcanology, 75(4), 1-16.

Le Bas, M.J., Le Maitre, R.W., Streckeisen, A., Zanettin, B., 1986. A chemical classification of volcanic rocks based on the total alkali-silica diagram. J. Petrol. 27 (3), 745-750.

Mandarano, M., Paonita, A., Martelli, M., Viccaro, M., Nicotra, E., Millar, I.L., 2016. Revealing magma degassing below closed-conduit active volcanoes: Geochemical features of volcanic rocks versus fumarolic fluids at Vulcano (Aeolian Islands, Italy). Lithos 248-251, 272-287.

Mangler, M., Petrone, C.M., Hill, S., Delgado-Granados, H., Prytulak, J., 2020. A pyroxenic view on magma hybridisation and crystallisation at Popocatépetl Volcano, Mexico. Frontiers Earth Sciences 8:362, doi: 10.3389/feart.2020.00362.

Masotta, M., Mollo, S., Freda, C., Gaeta, M., Moore, G., 2013. Clinopyroxene-liquid thermometers and barometers specific to alkaline differentiated magmas. Contrib. Mineral. Petrol. 166, 1545-1561.

Masotta, M., Mollo, S., Gaeta, M., Freda, C., 2016, Melt extraction in mush zones: The case of crystal-rich enclaves at the Sabatini Volcanic District (central Italy), Lithos, 248-251, 288-292. http://dx.doi.org/10.1016/j.lithos.2016.01.030.

Masotta, M., Pontesilli, A., Mollo, S., Armienti, P., Ubide, T., Nazzari, M., Scarlato, P., 2020. The role of undercooling during clinopyroxene growth in trachybasaltic magmas: Insights on magma decompression and cooling at Mt. Etna volcano. Geochimica et Cosmochimica Acta, 268, 258-276. https://doi.org/10.1016/j.gca.2019.10.009.

Mollo S., Putirka K., Misiti V., Soligo M., Scarlato P., 2013. A new test for equilibrium based on clinopyroxene-melt pairs: Clues on the solidification temperatures of Etnean alkaline melts at post-eruptive conditions. Chemical Geology, 352, 92-100, doi: 10.1016/j.chemgeo.2013.05.026.

Mollo S., Masotta M., 2014, Optimizing pre-eruptive temperature estimates in thermally and chemically zoned magma chambers, Chemical Geology, 368, 97-103. https://doi.org/10.1016/j.chemgeo.2014.01.007.

Mollo, S., Giacomoni, P.P., Coltorti, M., Ferlito, C., Iezzi, G., Scarlato, P., 2015. Reconstruction of magmatic variables governing recent Etnean eruptions: constraints from mineral chemistry and P-T-fO2-H2O modelling. Lithos 212-215, 311-320.

Mollo, S., Blundy, J., Scarlato, P., De Cristofaro, S.P., Tecchiato, V., Di Stefano, F., Vetere, F., Holtz, F., Bachmann, O., 2018. An integrated P-T-H2O-lattice strain model to quantify the role of clinopyroxene fractionation on REE+Y and HFSE patterns of mafic alkaline magmas: Application to eruptions at Mt. Etna. Earth Sci. Rev. 185, 32-56. https://doi.org/10.1016/j.earscirev.2018.05.014.

Mollo S., Ubide T., Di Stefano F., Nazzari M., Scarlato P., 2020a. Polybaric/polythermal magma transport and trace element partitioning recorded in single crystals: A case study of a zoned clinopyroxene from Mt. Etna. Lithos 356-357, 105382. https://doi.org/10.1016/j.lithos.2020.105382.

Mollo, S., Blundy, J., Scarlato, P., Vetere F., Holtz, F, Bachmann, O., Gaeta, M., 2020b. A review of the lattice strain and electrostatic effects on trace element partitioning between clinopyroxene and melt: Applications to magmatic systems saturated with Tschermak-rich clinopyroxenes. Earth-Science Reviews, 210, 103351. https://doi.org/10.1016/j.earscirev.2020.103351.

Nicotra, E., Giuffrida, M., Viccaro, M., Donato, P., D'Oriano, C., Paonita, A., De Rosa, R., 2018. Timescales of pre-eruptive magmatic processes at Vulcano (Aeolian Islands, Italy) during the last 1000 years. Lithos 316-317, 347-365.

Özdemir, Y., Blundy, J., Güleç, N., 2011. The importance of fractional crystallization and magma mixing in controlling chemical differentiation at Süphan stratovolcano, eastern Anatolia, Turkey. Contrib Mineral Petrol 162, 573–597. https://doi.org/10.1007/s00410-011-0613-8

Palummo, F., Mollo, S., De Astis, G., Di Stefano, F., Nazzari, M., Scarlato, P., 2020. Petrological and geochemical modeling of magmas erupted at Vulcano Island in the period 54-8 ka: Quantitative constraints on the sub-volcanic architecture of the plumbing system. Lithos, 374, 105715.

Peccerillo, A., Frezzotti, M.L., De Astis, G., Ventura, G., 2006. Modeling the magma plumbing system of Vulcano (Aeolian Islands, Italy) by integrated fluid-inclusion geobarometry, petrology, and geophysics. Geology 34 (1), 17-20.

Perinelli, C., Mollo, S., Gaeta, M., De Cristofaro, S.P., Palladino, D.M., Armienti, P., Scarlato, P., Putirka, K.D., 2016. An improved clinopyroxene-based hygrometer for Etnean magmas and implications for eruption triggering mechanisms. Am. Mineral. 101, 2774-2777.

Petrone, C.M., Bugatti, G., Braschi, E., Tommasini, S., 2016. Pre-eruptive magmatic processes re-timed using a non-isothermal approach to magma chamber dynamics. Nat. Commun. 7, 12946.

Petrone, C.M., Braschi, E., Francalanci, L., Casalini, M., Tommasini, S., 2018. Rapid mixing and short storage timescale in the magma dynamics of a steady-state volcano. Earth Planet. Sci. Lett. 492, 206-221.

Piochi, M., De Astis, G., Petrelli, M., Ventura, G., Sulpizio, R., Zanetti, A., 2009. Constraining the recent plumbing system of Vulcano (Aeolian Arc, Italy) by textural, petrological, and fractal analysis: The 1739 A.D. Pietre Cotte lava flow. Geochem. Geophys. Geosyst. 10 (No Q01009).

Putirka, K.D., 2008. Thermometers and barometers for volcanic systems. Rev. Mineral. Geochem. 69, 61-120.

Sparks, R.S.J., Sigurdsson, H., Wilson, L., 1977. Magma mixing: a mechanism for triggering acid explosive eruptions. Nature 267, 315-318.

Stelten, M.E., Cooper, K.M., Vazquez, J.A., Calvert, A.T., Glessner, J.J., 2015. Mechanisms and timescales of generating eruptible rhyolitic magmas at Yellowstone caldera from zircon and sanidine geochronology and geochemistry. Journal of Petrology, 56(8), 1607-1642.

Sun, C.G., Liang, Y., 2012. Distribution of REE between clinopyroxene and basaltic melt along a mantle adiabat: effects of major element composition, water, and temperature. Contrib. Mineral. Petrol. 163, 807-823. https://doi.org/10.1007/S00410-011-0700-X.

Sun, C., Graff, M., Liang, Y., 2017. Trace element partitioning between plagioclase and silicate melt: the importance of temperature and plagioclase composition, with implications for terrestrial and lunar magmatism. Geochim. Cosmochim. Acta 206, 273-295.

Sun, S.S., McDonough, W.F., 1989. Chemical and isotopic systematics of ocean basalts: implications for mantle composition and processes. In: Saunders, A. D., Norry, M. J. (eds) Magmatism in the Ocean Basins. Geol. Soc. Lond. Spec. Publ. 42, 313-345.

Szymanowski, D., Ellis, B.S., Wotzlaw, J.F., Buret, Y., von Quadt, A., Peytcheva, I., Bindeman, I.N., Bachmann, O., 2016. Geochronological and isotopic records of crustal storage and assimilation in the Wolverine Creek-Conant Creek system, Heise eruptive centre, Snake River Plain. Contributions to Mineralogy and Petrology, 171(12), 1-15.

Tecchiato, V., Gaeta, M., Mollo, S., Scarlato, P., Bachmann, O., Perinelli, C., 2018. Petrological constraints on the high-Mg basalts from Capo Marargiu (Sardinia, Italy): Evidences of cryptic amphibole fractionation in polybaric environments, Journal of Volcanology and Geothermal Research, 349, 31-46. https://doi.org/10.1016/j.jvolgeores.2017.09.007.

Ubide, T., Kamber, B.S., 2018. Volcanic crystals as time capsules of eruption history. Nat. Commun. 9, 326.

Ubide, T., Mollo, S., Zhao, J.-X., Nazzari, M., Scarlato, P., 2019a. Sector-zoned clinopyroxene as a recorder of magma history, eruption triggers, and ascent rates. Geochimica et Cosmochimica Acta, 251, 265-283. https://doi.org/10.1016/j.gca.2019.02.021.

Ubide, T., Caulfield, J., Brandt, C., Bussweiler, Y., Mollo, S., Di Stefano, F., Nazzari, M., Scarlato, P., 2019b. Deep Magma Storage revealed by Multi-Method Elemental Mapping of Clinopyroxene Megacrysts at Stromboli Volcano. Frontiers in Earth Science, 7:239. https://doi.org/10.3389/feart.2019.00239.

Ventura, G., 2013. Kinematics of the Aeolian volcanism (Southern Tyrrhenian Sea) from geophysical and geological data. In: Lucchi, F., Peccerillo, A., Keller, J., Tranne, C.A., Rossi, P.L. (Eds.), The Aeolian Islands Volcanoes. Geological Society, London, Memoirs 37, 3-11.

Welsch, B., Hammer, J., Baronnet, A., Jacob, S., Hellebrand, E., Sinton, J., 2016. Clinopyroxene in postshield Haleakala ankaramite: 2. Texture, compositional zoning and supersaturation in the magma. Contrib. Mineral. Petrol. 171, 6. https://doi.org/10.1007/s00410-015-1213-9.

Welsch, B., Faure, F., Bachèlery, P., Famin, V., 2009. Microcrysts record transient convection at Piton de la Fournaise volcano (La Réunion hotspot). Journal of Petrology, 50(12), 2287-2305.

Wood, B.J., Blundy, J.D., 1997. A predictive model for rare earth element partitioning between clinopyroxene and anhydrous silicate melt. Contrib. Mineral. Petrol. 129, 166-181. https://doi.org/10.1007/s004100050330.

Wood, B.J., Blundy, J.D., 2001. The effect of cation charge on crystal–melt partitioning of trace elements. Earth Planet. Sci. Lett. 188, 59-71. https://doi.org/10.1016/S0012-821X(01)00294-1.

Zanon, V., Frezzotti, M.L., Peccerillo, A., 2003. Magmatic feeding system and crustal magma accumulation beneath Vulcano Island (Italy): evidence from fluid inclusion in quartz xenoliths. J. Geophys. Res. 108, 2298-2301.

Figure captions

Fig. 1. Schematic map of Vulcano Island showing the locations of rock samples that are the subject of the present study (a). The map legend refers to Eruptive Epochs from 1 to 8, as reported in De Astis et al. (2013). Total alkali vs. silica (TAS) diagram after Le Bas et al. (1986) (b). The rock samples are classified as basalts, basaltic trachyandesites (shoshonites), trachyandesites (latites), trachytes, and rhyolites.

Fig. 2. Back-scattered electron (BSE) photomicrographs showing the most important textural features of clinopyroxene phenocrysts: Type 1 homogeneous crystals, Type 2 core/resorbed cores, Type 3 recharge bands, Type 4 mottled crystals, and Type 5 sector-zoned crystals.

Fig. 3. Electron microprobe intensity maps showing chemical zonation patterns of Type 2 core/resorbed cores, Type 3 recharge bands, and Type 5 sector-zoned crystals. For Type 3 recharge bands, note the development of Cr-rich concentric growth zones on early-formed clinopyroxene cores, within the clinopyroxene mantle, and at the clinopyroxene rim.

Fig. 4. Compositional ranges of clinopyroxene cores and mantles + rims are compared with the recharge bands. The Mg-number [Mg# = X_{Mg} / (X_{Mg} + X_{Fe2+}), where X is the cation fraction and all iron is expressed as Fe^{2+}] of clinopyroxene is plotted against the sum of diopside + hedenbergite components (i.e., ΣDiHd) and the concentration of TiO_2.

Fig. 5. Chondrite- (a) and primordial mantle- (b) normalized patterns of trace elements in clinopyroxene cores and mantles + rims. Normalization data are from Sun and McDonough (1989).

Fig. 6. Trace element patterns in clinopyroxene cores are compared with those from recharge bands. Elements have been selected in order to represent different geochemical groups: 1) light rare earth elements (LREE; Ce and Eu), 2) heavy rare earth elements (HREE; Yb), 3) high field strength

elements (HFSE; Zr), and 4) transition elements (TE; Cr and V). The Eu anomaly has been calculated as Eu/Eu* = Eu_N / (Sm_N × Gd_N)$^{0.5}$, where the subscript N indicates element concentrations normalized to the chondrite analysis reported in Sun and McDonough (1989).

Fig. 7. *P* and *T* histograms obtained by clinopyroxene-based barometric and thermometric calculations performed by equilibrating clinopyroxene core and bulk rock compositions as described in Palummo et al. (2020).

Fig. 8. Trace element patterns in clinopyroxene mantles + rims are compared with those from recharge bands. Elements have been selected in order to represent different geochemical groups: 1) light rare earth elements (LREE; Ce and Eu), 2) heavy rare earth elements (HREE; Yb), 3) high field strength elements (HFSE; Zr), and 4) transition elements (TE; Cr and V). The Eu anomaly has been calculated as Eu/Eu* = Eu_N / (Sm_N × Gd_N)$^{0.5}$, where the subscript N indicates element concentrations normalized to the chondrite analysis reported in Sun and McDonough (1989).

Fig. 9. Grey value diffusion profiles of two representative clinopyroxene crystals from shoshonite and rhyolite products (a). The diffusion profiles were calculated inside the blue area in the red box of the associated back-scattered electron (BSE) microphotograph. The analytical data set was modelled using the NIDIS code of Petrone et al. (2016) to quantify the time (Δt) elapsed between recharge band and the onset of eruption. Summary of all the time scales estimated through the application of NIDIS to clinopyroxene phenocrysts (b). Error bars represent minimum and maximum Δt uncertainties from NIDIS modeling.

Fig. 10. Cr/Yb ratios measured for clinopyroxene cores, recharge bands, and mantles + rims are comparatively displayed in order to place constraints on the recharge processes and mixing dynamics governing the evolutionary history of magmas (a). Working model for the extended plumbing system at Vulcano Island and the dynamic growth of clinopyroxene from magmas

exploring continuous physico-chemical changes due to the presence of interconnected reservoirs (b). Results from calculations based on the partitioning model of Mollo et al. (2018, 2020b) (c). The estimated values of La and Yb partitioning were used to invert the concentrations of REE in the melts from clinopyroxene cores and recharge bands. Different compositional vectors (i.e., colored arrows) represent the putative REE contents of end-member magmas in equilibrium with the more homogeneous clinopyroxene cores. The grey dashed symbols represent the putative REE contents of magmatic injections recorded by the more heterogeneous recharge bands.

Decoding multiple zoning patterns in clinopyroxene phenocrysts at Vulcano Island: A record of dynamic crystallization through interconnected reservoirs

[1]Flavia Palummo, [1,2]Silvio Mollo, [3]Chiara Maria Petrone, [4]Ben S. Ellis, [2]Gianfilippo De Astis, [2]Manuela Nazzari, [2]Piergiorgio Scarlato, [4]Olivier Bachmann

[1]Department of Earth Sciences, Sapienza - University of Rome, P. le Aldo Moro 5, 00185 Roma, Italy

[2]Istituto Nazionale di Geofisica e Vulcanologia - Department Roma 1, Via di Vigna Murata 605, 00143 Roma, Italy

[3]The Natural History Museum, Department of Earth Sciences, Cromwell Road, SW7 5BD, London, United Kingdom

[4]Institute of Geochemistry and Petrology, ETH Zürich, 8092 Zurich, Switzerland

Corresponding author:

Flavia Palummo

Sapienza-Università di Roma

Dipartimento di Scienze della Terra

P.le Aldo Moro 5

00185 Roma, Italy

e-mail flavia.palummo@uniroma1.it

Abstract

Here we document how the different growth features and intracrystalline distributions of both major and trace cations in clinopyroxene phenocrysts are important recorders of the intricate magma dynamics at Vulcano Island (Aeolian Arc, Italy). The compositions of clinopyroxene phenocrysts from products erupted over the last ~54 ka cluster at different degrees of evolution, paralleling the polybaric-polythermal differentiation of mantle-derived mafic magmas into more evolved silicic melts. The hotter lower crust is the most favorable location for the storage of mafic magmas and the early crystallization of diopsidic ($Mg\#_{91}$) clinopyroxene (P_{max} ≈ 750 MPa and T_{max} ≈ 1,220 °C). Diopsidic phenocrysts are depleted in both rare earth elements (REE) and high field strength elements (HFSE) but are enriched in transition elements (TE). The transfer and accumulation of primitive magmas in the colder upper crustal regions lead to the formation of an interconnected series of more differentiated magmatic reservoirs (P ≈ 100-450 MPa and T ≈ 1,100-1,180 °C) hosting discrete populations of clinopyroxene ($Mg\#_{84-85}$) with a broad spectrum of zonations and dissolution features. Recharge bands in clinopyroxene are markers of multiple inputs of primitive REE-HFSE-poor, TE-rich magmas from depth. Augitic phenocrysts ($Mg\#_{82}$) with strong negative Eu anomaly and REE + HFSE enrichments crystallizes from highly differentiated trachytic and rhyolitic melts stored at very shallow crustal conditions (P ≤ 50 MPa and T ≤ 1,100 °C). These silicic reservoirs represent residual melts trapped-extracted from crystal-dominated mush regions in the uppermost part of the plumbing system. The residence time of clinopyroxene increases from ~0.1 to ~44 years from basalt to rhyolite, together with an increasing number of recharge bands. The mineral assemblage in more silicic and viscous mush melts is sufficiently resilient to record numerous mafic injections and high degrees of magma mixing, hybridization, and crystallization before eruption. Overall, the compositional zoning pattern of clinopyroxene presents a picture of plumbing system that extends through the crust and is

characterized by distributions of melts and crystals which are progressively more evolved and heterogeneous in both space and time.

Keywords: clinopyroxene; Vulcano Island; magma dynamics; magma mixing, hybridization, and crystallization; plumbing system architecture.

1. Introduction

Vulcano Island (Aeolian Arc, Italy) is characterized by a broad spectrum of clinopyroxene-bearing eruptive products, with a general temporal variation in compositions from basalt to rhyolite (e.g., Keller, 1980; Ellam et al., 1988; De Astis et al., 1997, 2013). The volcanic history is controlled by the continuous supply of mafic magma from mantle depths into shallow crustal levels, where high degrees of mixing and fractional crystallization lead to the formation of more differentiated reservoirs, together with occasional assimilation of small amounts of crustal materials (Bullock et al., 2019; Costa et al., 2020, 2021; De Astis et al., 1997; Gioncada et al., 1998, 2003; Forni et al., 2015; Nicotra et al., 2018; Palummo et al., 2020; Peccerillo et al., 2006; Piochi et al., 2009; Zanon et al., 2003).

The picture emerging from geophysical, volcanological, and petrological considerations is entirely consistent with a plumbing system that extends vertically through the crust and is characterized by a multi-faceted geometry (Clocchiatti et al., 1994; De Astis et al., 1997, 2013; Peccerillo et al., 2006; Zanon et al., 2003; Costa et al., 2020, 2021; Nicotra et al., 2018; Palummo et al., 2020). Considering this articulated architecture, we infer that complex zoning patterns in clinopyroxene phenocrysts have the potential to integrate a broad range of spatio-temporal information, providing an important record of the physico-chemical changes of magmas (Forni et al., 2016; Mollo et al., 2015, 2020a; Szymanowski et al., 2016; Ubide et al., 2019a; Welsch et al., 2016;). Clinopyroxene is an important recorder of mixing, hybridization, and differentiation mechanisms that control the dynamics of magma within the crust and, ultimately, preserves a detailed record of the magma recharge history (Di Stefano et al., 2020; Dunworth et al., 2001; Gioncada et al., 2005; Mangler et al., 2020; Tecchiato et al., 2018; Ubide et al., 2019b). Deconvolution of systematic zoning patterns in clinopyroxene may help to reconstruct the recharge dynamics of magma reservoirs, as well as the time and length scales required to mobilize magmas before eruptions (e.g., Petrone et al., 2016, 2018; Ubide and Kamber, 2018). Additionally, the stability field of clinopyroxene encompasses a broad range of *P*-*T*-*X* conditions, from mantle depths to very shallow crustal levels, and its crystallization may strictly control the geochemical evolution of solidifying melts in terms of major and trace element contents (e.g., Beard et al., 2019; Masotta et al., 2013; Mollo and Masotta, 2014; Mollo et al., 2015; Putirka et al., 2008; Perinelli et al., 2016; Sun and Liang, 2012, 2017).

Although the investigation of clinopyroxene complexity and diversity can be a powerful tool to gain information on the dynamics of multi-stage plumbing systems, no studies have yet categorized and decoded the complex zoning patterns of clinopyroxene at Vulcano Island. For this purpose, we present a broad compositional data set for major and trace elements analyzed in clinopyroxene phenocrysts from twenty-one basaltic-to-rhyolitic products representative of the volcanism occurred from ~54 ka to historical times. A detailed petrological description, geochemical modeling, and petrogenetic significance of fifteen products with ages in the range of ~8-54 ka can be found in Palummo et al. (2020). Here the data set has been integrated with six latitic and trachytic rock samples, which extend the eruptive period to the youngest product of La Fossa cone dated at 1739 CE on the basis of contemporary historical chronicles (see De Astis et al., 2013 and references therein). Interrogation of the textural and compositional changes of clinopyroxene reveals that zonations are intrinsic to the process of magma solidification, thus providing a more comprehensive view of the geochemical evolution of multiple magma batches undergoing polybaric-polythermal crystallization under open-system conditions. The interpretation and modeling of major and trace cation distributions in clinopyroxene affords considerable insight into the mechanisms and timescales by which multiple magma storage regions developed at variable depths and then interacted with each other, before feeding volcanic eruptions.

2. Volcanological background

Vulcano Island is an active volcanic system located in the southernmost sector of the Aeolian Archipelago (Fig. 1a), a Quaternary volcanic arc generated by subduction of the oceanic Ionian plate underneath the Calabrian arc (Ventura, 2013). The Aeolian Archipelago consists of seven islands and nine seamounts forming a ring-like structure, whose northwestern sector lies on the oceanic crust of the Tyrrhenian abyssal plain and eastern and southern sectors on ~18-25 km thick continental crust of the Calabro-Peloritano basement (De Astis et al., 1997). The three islands of Vulcano, Lipari, and Salina are part of a volcanic complex that developed within a graben-like structure controlled by the NNW-SSE strike-slip Tindari–Letojanni fault system (Gioncada et al., 2003; Ventura, 2013). Accordingly, the structural pattern of Vulcano Island is dominated by major NW–SE- to NNW–SSE-striking fault system (De Astis et al., 2013). The island has a total surface area of ~22 km^2, its base lies at an average depth of ~1 km b.s.l. and the maximum height is ~499 m a.s.l. at Monte Aria (De Astis et al., 2013 and references therein). The calc-alkaline affinity of the erupted products is related to subduction processes due to the presence of a NW-dipping Benioff-Wadati zone (Davì et al., 2009). The subaerial volcanic activity at Vulcano Island started 127 ka in the southern sector of the island with the building of Primordial Vulcano stratocone (Fig. 1a; Mandarano et al., 2016). Afterwards, the volcanic edifice was affected by volcano-tectonic collapses occurring at 100, 80, and 50 ka. The first two collapses were related to the formation of Il Piano caldera, whereas the third collapse was associated to the early phases of La Fossa caldera (Fig. 1a; Davì et al., 2009). The last eruption occurred from August 1888 to March 1890 at La Fossa cone (Keller, 1980). This is a 391-m-high tuff cone mainly developed through phreatomagmatic eruptions and minor lava effusions (Dellino et al., 2011). The peninsula of Vulcanello (Fig. 1a) formed as a new islet in Roman times. This peninsula represents the northernmost structure located along the northern border of La Fossa caldera, consisting of a lava platform and three nested scoria cones with alignment ENE-WSW (Davì et al., 2009; De Astis et al., 1997, 2013). According to De Astis et al. (2013), the overall eruptive history of Vulcano Island can be divided in eight Eruptive Epochs (Fig. 1a) that represent the principal building stages of the volcanic edifice interrupted by periods of quiescence, sometimes also associated with volcano-tectonic collapses (e.g., Il Piano Caldera, La Fossa Caldera).

3. Sampling and analytical methods

3.1. Sample selection

The magmatic activity of the last ~54 ka at Vulcano Island has been investigated through textural and chemical (major and trace elements) analyses of clinopyroxene phenocrysts (i.e., crystals with longest size dimensions >0.3 mm; Lanzafame et al., 2013 and references therein) from various volcanic rocks, mainly lavas and scoriae, erupted during the considered timespan.

A total of twenty-one rock samples, were collected from several strategic sectors and formations, in which the eruptive units were identified on the basis of their different lithostratigraphic and compositional characteristics (Table 1). The rock samples represent the last Eruptive Epochs 5, 6, 7, and 8 (i.e., between ~54 ka and 1739 CE; De Astis et al., 2013) of Vulcano Island (Fig. 1a). According to the TAS diagram (Total Alkali vs. Silica; Le Bas et al., 1986; Fig. 1b), samples are classified as five distinct groups: 1) basalts ($SiO_2 \approx$ 48.9-51.4 wt.%; $Na_2O + K_2O \approx$ 4.3-4.6 wt.%), 2) basaltic trachyandesites (i.e., shoshonites; $SiO_2 \approx$ 52.2-54.4 wt.%; $Na_2O + K_2O \approx$ 7.3-7.9 wt.%), 3) trachyandesites (i.e., latites; $SiO_2 \approx$ 54.2-57.5 wt.%; $Na_2O + K_2O \approx$ 7.1-9.2 wt.%), 4) trachytes ($SiO_2 \approx$ 62.4-68.4 wt.%; $Na_2O + K_2O \approx$ 8.3-9.1 wt.%) and 5) rhyolites ($SiO_2 \approx$ 71.0-73.7 wt.%; $Na_2O + K_2O \approx$ 8.5-8.7 wt.%). Bulk rock analyses of rock samples and a detailed description of their eruptive epochs are reported in Supplementary Material 1.

3.2. Analytical methods

Textural and chemical microanalyses on clinopyroxene phenocrysts were carried out with a field emission gun-scanning electron microscope (FE-SEM) and an electron microprobe (EMP), respectively, installed at the High Pressure - High Temperature (HP-HT) Laboratory of Experimental Volcanology and Geophysics of the Istituto Nazionale di Geofisica e Vulcanologia (INGV) in Rome (Italy). Trace element analyses of clinopyroxene phenocrysts were determined by laser ablation-inductively coupled plasma-mass spectrometry (LA-ICP-MS) at the Institute of

Geochemistry and Petrology, ETH Zürich (Switzerland). Conditions used for analyses are reported in Supplementary Material 1.

4. Results

4.1. Clinopyroxene textural and chemical zonation

Clinopyroxene is the ubiquitous mineral phase in all the investigated samples and usually the length of its longest axis is comprised between 0.3 and 1 mm. Distinctive and complex textural changes are observed for clinopyroxene by combining grey level distribution of high-contrast BSE (backscattered electron) images (Fig. 2) and X-ray microprobe maps in false colors (Fig. 3). On this basis, five main clinopyroxene populations have been identified (Table 1):

- Type 1: unzoned phenocrysts. Euhedral phenocrysts with homogeneous compositions are extremely rare in the erupted products (Fig. 2). Unzoned phenocrysts are prevalently found in basalts and some primitive shoshonites, whereas they are absent in latites, trachytes and rhyolites (Table 1);
- Type 2: cores/resorbed cores. Several phenocryst cores are heralds of an early stage of crystallization and one or more resorbed cores preserve evidence of dissolution. In BSE photomicrographs, subhedral-to-anhedral dark grey (low mean atomic number) crystal portions are surrounded by light grey (high mean atomic number) mantles + rims (Figs. 2 and 3). The innermost parts of resorbed cores are unaffected by dissolution features, showing compositions identical to those of the homogeneous cores. Accordingly, resorbed cores represent early-formed cognate clinopyroxenes that crystallized in equilibrium with the resident magma before partial dissolution and recrystallization caused by injections of hotter recharge melts;
- Type 3: recharge bands. Dark grey concentric growth zones developed within the clinopyroxene light grey mantle (Figs. 2 and 3). These recharge bands show sharp interfaces and are composed of continuous, planar segments, each of which responds to growth under a

certain crystal face. Within any given concentrically zoned overgrowth, the BSE intensity changes across the growth crystal boundary in the same sense, denoting that recharge bands are time-equivalent growth surfaces forming by supply of new magma to the advancing crystalline layer (Fig. 2 and 3). The darker BSE intensity of clinopyroxene cores, resorbed cores, and recharge bands is ascribed to higher contents of MgO and Cr_2O_3 and lower contents of Al_2O_3 and FeO compared to phenocryst mantles + rims (Fig. 3). Phenocrysts with recharge bands are more common in trachyte and rhyolite samples than in other rock types (Table 1);

- Type 4: mottled phenocrysts. Aggregation and/or conjoining of mutually touching resorbed crystals (Fig. 2), with indistinct boundaries due to the effect of dissolution (Dunworth et al., 2001). Mottled crystals are found from shoshonitic-to-rhyolitic products and their frequency increases with increasing degree of melt differentiation (Table 1). Irregular crystal portions show contrasting compositions, with both dark grey and light grey domains that are similar to those of resorbed cores and testify to dissolution and recrystallization of crystal aggregates during magma mixing;
- Type 5: sector-zoned phenocrysts. Sector zoning in clinopyroxene consists of hourglass (or basal) forms {-1 1 1} and prism forms {*h k* 0}, including {1 0 0}, {1 1 0}, and {0 1 0} faces. Sectors are identified by changes in BSE intensity from darker hourglass to lighter prism (Fig. 2) and are found only in shoshonites and latites (Table 1). Hourglass sectors grow faster along the c-axis, whereas prism sectors grow slower perpendicular to the *c* crystallographic axis (e.g., Ubide et al., 2020 and references therein). A growth sector boundary marks the interface between adjacent {-1 1 1} and {*h k* 0} forms, showing shapes either straight or slightly curved due to local variations in growth rates on the two faces (Fig. 2). Hourglass sectors are enriched in SiO_2 + MgO and depleted in Al_2O_3 + FeO_{tot} compared to prism sectors (Fig. 3). Both these sectors are sometimes crossed by concentric banding with sharp interfaces subparallel to the growing sector boundary (Fig. 2).

4.2. Clinopyroxene major elements

The whole data set derived for clinopyroxene major and trace element analyses is reported in Supplementary Material 1, together with variation diagrams where all the compositions of clinopyroxene cores, mantles + rims, and recharge bands are displayed on single plots.

Using the classification scheme reported in the review of Mollo et al. (2020b), we have calculated clinopyroxene cation fractions (*X*) and components (i.e., diopside, Di, $CaMgSi_2O_6$; hedenbergite, Hd, $CaFeSi_2O_6$; enstatite, En, $Mg_2Si_2O_6$; ferrosilite, Fs, $Fe_2Si_2O_6$), for each crystal population. Clinopyroxene cores are classified as diopside to diopside-augite (Di_{66-83}-Hd_{9-19}-En_{7-11}-Fs_{1-3}), whereas recharge bands and mantles + rims can be classified as augite (Di_{64-73}-Hd_{13-20}-En_{11-12}-Fs_{2-4} and Di_{65-61}-Hd_{19-21}-En_{13-16}-Fs_{4-5}, respectively).

Fig. 4 shows the Mg-number [Mg# = X_{Mg} / (X_{Mg} + X_{Fe2+}), where *X* is the cation fraction and all iron is expressed as Fe^{2+}] of clinopyroxene plotted against the sum of Di + Hd components (i.e., ΣDiHd) and the concentration of TiO_2 in phenocryst cores and phenocryst mantles + rims compared with recharge bands. The most relevant crystal chemical changes are presented here as average compositions of single samples. This comparison highlights that ΣDiHd decreases from clinopyroxene cores + recharge bands (0.80-0.88 on average) to clinopyroxene mantles + rims (0.76-0.79 on average). Conversely, the concentration of TiO_2 increases from 0.2 to 0.6 wt.% on average, as the growth of clinopyroxene takes place in more differentiated melt compositions (Fig. 4).

The Mg# of phenocryst cores abruptly decreases from basalts ($Mg\#_{91}$ on average) to shoshonites + latites ($Mg\#_{84-85}$ on average) to trachytes ($Mg\#_{82}$ on average) to rhyolites ($Mg\#_{78}$ on average), resembling the geochemical evolution of the host rocks (compare Figs. 1 and 4). Importantly, clinopyroxene is an early liquidus phase and its core is in equilibrium with the bulk rock composition as previously determined by Palummo et al. (2020). The equilibrium condition between clinopyroxene core and bulk rock compositions has been tested by the Fe-Mg exchange

(0.28 ± 0.08) of Putirka (2008), in conjunction with models based on the difference (Δ) between measured vs. predicted ΣDiHd components (Mollo et al., 2013; Mollo and Masotta, 2014) and thermodynamically-predicted partition coefficients for Na (Blundy et al., 1995) and Ti (Mollo et al., 2018, 2020). Due to the effects of magma mixing and hybridization phenomena, the equilibrium partitioning of Fe, Mg, Ti, and Na cations between the early-formed core and host magma has been restored by adding/subtracting to the bulk rock minimum amounts of minerals along the olivine-clinopyroxene-plagioclase cotectic (see supplementary data in Appendix A of Palummo et al., 2020). ΣDiHd decreases with proceeding magma differentiation from basalts (0.88 ± 0.01 on average) to latites + shoshonites + less differentiated trachytes (0.83 ± 0.01 on average) to more differentiated trachytes + rhyolites (0.80-0.82 ± 0.01 on average). The amount of TiO_2 in clinopyroxene remains almost identical from shoshonite to rhyolite (0.3-0.4 wt.% ± 0.04 on average). Conversely, diopsidic phenocrysts from mantle-derived basaltic rocks are characterized by lower TiO_2 concentrations (0.2 ± 0.04 wt.% on average; Fig. 4).

The entire compositional range of recharge bands is between $Mg\#_{80}$ and $Mg\#_{88}$, with an average of $Mg\#_{82}$ (Fig. 4). Recharge bands are more differentiated than diopsidic cores found in mantle-derived basalts and mimic the chemistry of clinopyroxene cores from shoshonites, latites, and trachytes. This compositional feature supports the idea of a polybaric-polythermal magmatic differentiation within the crust that proceeds in cooperation with recurrent mixing and hybridization processes (Gioncada et al., 2003). A small population of recharge bands from rhyolites (~13% of the whole data set) exhibits low TiO_2 abundances (≤0.2 wt.%; Fig. 4) resulting from the increased stability of titanomagnetite in the upper crust (Palummo et al., 2020).

Clinopyroxene mantles + rims from basalts to rhyolites depict a narrower and more evolved compositional range of $Mg\#_{75\text{-}78}$ relative to phenocryst cores + recharge bands (Fig. 4). The amount of ΣDiHd significantly decreases in clinopyroxene mantles + rims, especially due to strong CaO depletion caused by the incipient late-stage crystallization of feldspar (plagioclase + sanidine) during magma cooling and decompression (De Astis et al., 2013). Clinopyroxene mantles + rims from basalts ($Mg\#_{78}$ on average) remain systematically less differentiated than those ($Mg\#_{76}$ on average) from other rocks. Most of the compositions of mantles + rims from shoshonites to rhyolites overlap, without displaying any clear evolutionary trend neither for ΣDiHd or TiO_2 (Fig. 4). Clinopyroxene mantles + rims from latites ($Mg\#_{75}$ on average) are slightly more evolved than those from rhyolites ($Mg\#_{76}$ on average), in agreement with the increased number of recharge bands observed in phenocrysts from silicic host rocks and suggesting recurrent inputs of fresh and more primitive magmas from depth (Table 1).

4.3. Clinopyroxene trace elements

The chondrite-normalized patterns (Sun and McDonough, 1989) of rare earth elements (REE) in clinopyroxenes exhibit sub-parallel trends, shifting towards progressive trace element enrichments from basalt to rhyolite according to the more differentiated character of magma (Fig. 5). The concentration of light REE (LREE) is typically higher than that of heavy REE (HREE). Clinopyroxene mantles + rims exhibit lower LREE/HREE ratios (i.e., the normalized La/Yb ratio; La_N/Yb_N) and more pronounced negative Eu anomalies (i.e., $Eu/Eu^* = Eu_N/(Sm_N \times Gd_N)^{0.5}$) than clinopyroxene cores and recharge bands (Fig. 5). From basalts to rhyolites, both Eu/Eu* and La_N/Yb_N measured in clinopyroxene cores decrease from ~0.92 ± 0.06 to ~0.61 ± 0.06 on average and from ~2.8 ± 0.2 to ~2.3 ± 0.2 on average, respectively. In clinopyroxene mantles + rims, the values of Eu/Eu* and La_N/Yb_N further decrease to ~0.5 and ~2.0, respectively, responding to the abundant crystallization of feldspar at the late stage of melt differentiation.

The primordial mantle-normalized patterns (Sun and McDonough, 1989) of trace elements in clinopyroxenes show typical features of arc magmas, with enrichments in large ion lithophile element (LILE) to high field strength element (HFSE) ratios (Fig. 5). Both clinopyroxene cores, recharge bands, and mantles + rims display troughs at Ba, K, Nb, P, Zr, and Ti in (Fig. 5). The concentration of incompatible elements in clinopyroxene cores shows a marked increase from basalts to rhyolites, while the incompatible element concentrations partly overlap in clinopyroxene mantles + rims from trachytes to rhyolites (Fig. 5). Negative spikes of K, Sr, P, and Ti are more marked in clinopyroxene cores from trachytes and rhyolites, in agreement with the phase assemblage (i.e., feldspar + oxide ± apatite) that characterizes the more differentiated eruptions.

From clinopyroxene cores to recharge bands to mantles + rims, the amount of compatible transition elements (TE) decreases from 1,005 to 242 ppm and from 99 to 89 ppm for Cr and Ni, respectively. In particular, Cr is extremely high in phenocrysts from basalts (2,131 ± 102 ppm on average) relative to those from rhyolites (440 ± 107 ppm on average) and is well correlated with the Mg# of clinopyroxene. Conversely, V, Co, and Zn behave like incompatible elements and their average concentration increases with the host rock differentiation from 126 to 209 ppm, from 41 to 54 ppm, and from 40 to 76 ppm, respectively (Supplementary Material 1).

Scandium is highly compatible in clinopyroxene (cf. Mollo et al., 2020a) and its concentration decreases from clinopyroxene cores (87 ± 4 ppm on average) to mantles + rims (76 ± 2 ppm on average), resembling the progressive melt depletion with proceeding crystallization (Supplementary Material 1).

5. Discussion

5.1. The geochemical evolution of clinopyroxene

Fig. 6 shows that the differentiation path of magmas is faithfully recorded by major and trace element contents of clinopyroxene cores from products with different degrees of evolution. Diopsidic cores ($Mg\#_{91}$) from mantle-derived basalts support the idea of a unique deep level of magma, whose bulk composition is characterized by low incompatible LREE (i.e., Ce) and HFSE (i.e., Zr) concentrations, in conjunction with high TE/HREE ratios (i.e., Cr/Yb and V/Yb ratios; Fig. 6). Forsteritic ($Fo_{87–91}$) olivines are in equilibrium with diopsidic cores and the homogenization temperature of olivine-hosted melt inclusions indicates crystallization at $T \approx$ 1,190–1,250 °C (Gioncada et al., 1998). Thermobarometric constraints and thermodynamic calculations based on the equilibrium between clinopyroxene core and bulk rock compositions (see above), confirm that diopsidic phenocrysts equilibrated with primitive basaltic magmas at P_{max} ≈ 750 MPa and T_{max} ≈ 1,220 °C (Fig. 7). Primitive basaltic magmas are inferred to originate at mantle depths via partial melting of a depleted peridotitic source veined by metasomatic, clinopyroxene-rich regions (Kamenetsky and Clocchiatti, 1996). The occurrence of a mafic mineral assemblage in equilibrium with deep-seated magmas is in accordance with a Moho depth estimated at ~21–25 km, corresponding to P ≈ 620–740 MPa for a continental crust density of 2.7 g/cm^3 (Peccerillo et al., 2006 and references therein).

The *P-T* array traced by the crystallization of clinopyroxene changes significantly as the basaltic magmas migrate and differentiate towards two shallower and colder storage regions hosting 1) shoshonitic, latitic, and less differentiated trachytic melts at P ≈ 100-450 MPa and T ≈ 1,100-1,180 °C and 2) highly differentiated trachytic and rhyolitic melts at $P \leq 50$ MPa and $T \leq 1{,}100$ °C (Fig. 7). As P decreases, the stability field of clinopyroxene decreases in favor of olivine crystallization (Palummo et al., 2020) and the clinopyroxene composition shifts from diopside-augite ($Mg\#_{84\text{-}85}$) to augite ($Mg\#_{82\text{-}77}$). More evolved magmas residing at shallower crustal conditions are saturated with feldspar and titanomagnetite at $T < 1{,}100$ °C (Fig. 7). The abundant formation of plagioclase is also promoted by cooling-decompression regimes related to H_2O exsolution and degassing (cf. Mandarano et al., 2016 and references therein). Ce and Zr enrichments in clinopyroxene cores from basalts to rhyolites are in accord with the progressive differentiation of magma (Fig. 6). The Mg# of clinopyroxene plotted against the TE/HREE ratio highlights that basalts, shoshonites + latites, and trachytes + rhyolites cluster at different degrees of evolution (Fig. 6). In particular, the abrupt decrease of Cr/Yb ratio from basalts (9,500-12,500) to shoshonites + latites (500-2,500) to trachytes + rhyolites (100-500; Fig. 6) confirms the early and extensive crystallization of mafic minerals (olivine + clinopyroxene), in which Cr is prevalently incorporated (e.g., Tecchiato et al., 2018). As the composition of magma evolves, the concentration of incompatible Ce and Zr elements progressively increases in clinopyroxene cores. At the same time, the increasing stability of plagioclase leads to stronger negative Eu anomalies (Eu/Eu*) and lower LILE/HREE ratios (i.e., Sr/Yb ratios), especially for trachytes and rhyolites (Fig. 6). Silicic magmas are stored in upper and colder crustal environments located at $P \leq 50$ MPa (Fig. 7) and, likely, are generated by the extraction of interstitial melts from crystal-rich (mushy) reservoirs. Abundant segregation of feldspar phenocrysts is inferred to be responsible for the development of distinct magma-mush pockets (Palummo et al., 2020; Nicotra et al., 2018). Feldspar-liquid separation processes can be also favored by second boiling of the melt and consequent volatile exsolution of a fluid phase at $T \approx 860$–1,100 °C and H_2O concentrations in excess of ~2.5–4.0 wt.% (Gioncada et al., 2003; Costa et al., 2020; Palummo et al., 2020).

Intracrystalline heterogeneities in clinopyroxene are recorders of recurrent magma recharge and mixing events (Type 3 recharge bands; Figs. 2 and 3), generally accompanied by multi-stage crystal dissolution phenomena (Type 2 resorbed cores and Type 4 mottled aggregates; Figs. 2 and 3). Resorbed cores are interpreted as evidence of corrosion by thermal and/or chemical disequilibrium with the melt. This open-system behavior is caused by the injection of hotter and more mafic magmas into compositionally distinct reservoirs within the crust (Bullock et al., 2019; Costa et al., 2020; De Astis et al., 2013; Nicotra et al., 2018). Concentric Cr zonation in clinopyroxene indicates subtle modulations in the history of melt composition involved in clinopyroxene growth (Fig. 3). Several clinopyroxene phenocrysts contain Cr-rich resorbed cores that likely formed by replenishment of the crystallizing reservoir. These cores were partially dissolved during protracted storage at magmatic temperature and finally incorporated into the new recharge melt (Ubide and Kamber, 2018; Mollo et al., 2020a). Owing to the broad compositional range of clinopyroxene-bearing magmas (Fig. 1a), the destabilization-dissolution of clinopyroxene cores is probably controlled by mutual thermal and chemical effects caused by the transport of crystals through the upper crust (e.g., Mollo and Masotta, 2014; Forni et al., 2016, 2018). In a similar fashion, the formation of Type 3 concentrically zoned phenocrysts can be ascribed to repeated recharge events that are inferred to be drivers of convective dynamics in crustal storage regions (Bergantz et al., 2015). Given that some Cr-rich bands developed at the clinopyroxene rim (Fig. 3), it is plausible that the eruption was triggered by the injection of mafic magma (Ubide and Kamber, 2018; Petrone et al., 2018). Magma mixing is frequently suggested as an effective eruption trigger (Sparks et al., 1977; Druitt et al., 2012) and is sometimes associated with volatile exsolution during magma ascent from depth towards the surface (Cashman et al., 2017).

Fig. 8 shows that recharge bands ($Mg\#_{81-85}$) are markers of primitive REE-HFSE-poor, TE-rich magmas injecting into more differentiated REE-HFSE-rich, TE-poor domains, where clinopyroxene mantles + rims ($Mg\#_{75-78}$) developed at the late stage of magma mixing-hybridization. The abrupt decrease of averaged Sr/Yb ratio from 89 (recharge bands) to 42 (mantles + rims) and the strong negative Eu anomaly (Fig. 8) confirm that most of the evolutionary path is controlled by incipient plagioclase crystallization (De Astis et al., 2013; Nicotra et al., 2018). In view of this magma compositional shift, the concentration of Zr markedly increases up to 52 ppm in clinopyroxene mantles + rims, whereas the Cr/Yb ratio reaches a minimum of 0.5 (Fig. 8). It is also interesting to note that clinopyroxene mantles + rims from trachytes and rhyolites appear less differentiated than expected for silicic magmas, mostly showing major and trace element contents similar to the crystal cargo of basaltic and shoshonitic products (Fig. 8). This compositional observation matches with the numerous recharge bands enclosed within clinopyroxenes from trachytes and rhyolites (Table 1), attesting to continuous replenishment of the shallow plumbing system and consequent magma hybridization within the crystal mush (e.g., Forni et al., 2016).

Type 5 sector-zoned clinopyroxene phenocrysts are sporadically found in shoshonites and latites (Figs. 2 and 3). Si-Mg-rich hourglass forms {-1 1 1} are depleted in REE (e.g., Ce = 14 ± 1.2 and Yb = 1 ± 0.01 ppm on average) and HFSE (e.g., Hf = 1 ± 0.01 ppm and Zr = 19 ± 1.3 ppm on average) relative to Al-Fe-rich prism forms {*h k* 0} (e.g., Ce = 31 ± 3.1 ppm, Yb = 3 ± 0.02 ppm, Zr = 36 ± 3.4 ppm, and Hf = 2 ± 0.02 ppm on average). The intracrystalline distribution of major cations among the different sectors agrees with that observed for sector-zoned augites at Mt. Etna (Downes, 1974; Ubide et al., 2019a) and Stromboli (Ubide el al., 2019b). Sectoral partitioning of

REE and HFSE cations is strictly controlled by both charge-balanced and -imbalanced configurations taking place in the structural sites of {-1 1 1} and {*h k* 0} sectors as the number of Al cations in tetrahedral coordination increases (Ubide et al., 2019a). The magnitude of sectoral partitioning at Vulcano Island is very similar to that measured at Stromboli, whereas the compositional difference between {-1 1 1} and {*h k* 0} sectors is much more marked for the clinopyroxene populations at Mt. Etna. For example, the $Al_2O_{3\{-1\ 1\ 1\}}/Al_2O_{3\{h\ k\ 0\}}$ ratios in phenocrysts at Vulcano Island, Stromboli, and Mt. Etna are on the order of 0.88, 0.81, and 0.58, respectively. According to literature, the differential partitioning of cations between {-1 1 1} and {*h k* 0} faces is proportional to the degree of undercooling that, in turn, governs the growth of clinopyroxene under different magmatic conditions (Kouchi et al. 1983; Welsch et al., 2016; Ubide el al., 2019b; Giuliani et al., 2020; Masotta et al., 2020). Ubide el al. (2019b) compared the stronger sector zonation of clinopyroxenes from Mt. Etna with the weaker sector zonation of crystals from Stromboli. The authors concluded that the slow growth of clinopyroxene at Stromboli was generated by magmas undergoing very low degrees of undercooling comprised between 10 and 20 °C. Building on constraints from clinopyroxene growth experiments carried out by Kouchi et al. (1983), we observe that $Al_2O_{3\{-1\ 1\ 1\}}/Al_2O_{3\{h\ k\ 0\}}$ ratios for phenocrysts from Vulcano Island and Stromboli are generated by a degree of undercooling of ~13 °C. On the other hand, Masotta et al. (2020) have experimentally documented that sectoral partitioning of natural phenocrysts from Mt. Etna is caused by higher degrees of undercooling, mostly comprised between 23 and 32 °C. In this regard, magma dynamics driving the eruption of shoshonites-latites at Vulcano Island can be interpreted as the effect of sluggish crystallization kinetics under growth-dominated regimes during very slow magma ascents (Ubide el al., 2019b). It is also plausible that sector-zoned clinopyroxenes originated by small-scale convective transport of crystals through thermally heterogeneous magma reservoirs (cf. Welsch et al., 2009) that are located within the plumbing system at ~10-17 km of depth (De Astis et al., 2013; Palummo et al., 2020).

5.2. Timescales record of pre-eruptive processes

As discussed above, high-Mg# and Cr_2O_3-rich recharge bands of Type 3 clinopyroxene phenocrysts (Figs. 2 and 3) indicate crystallization from 1) a high-*T*, mafic magma that is recorded by the recharge band and 2) a low-*T*, resident magma which is homogenized by mixing and hybridization after the mafic injection. Fe-Mg compositional zoning profiles in clinopyroxene phenocrysts have been examined to quantify the crystal residence time (Δt) via elemental diffusion chronometry using the NIDIS (Non-Isothermal Diffusion Incremental Step) model of Petrone et al. (2016). BSE microphotographs and greyscale profiles are used as proxies for Fe-Mg compositional zoning boundary layers along transects normal to the recharge band-rim interface (see Supplementary Material 2). The crystallization temperatures of clinopyroxene recharge bands and rims in equilibrium with different melt components have been calculated by using thermobarometric models based on exchange equilibria (cf. Palummo et al., 2020; see also temperature histograms in Supplementary Material 1): 1) 1,200-1,220 °C (high-Mg# recharge band) and 1,190-1,200 °C (low-Mg# rim) for basalts, 2) 1,130-1,180 °C (high-Mg# recharge band) and 1,100-1,160 °C (low-Mg# rim) for shoshonites, latites, and trachytes, and 3) 1,090-1,100 °C (high-Mg# recharge band) and 1,080-1,090 °C (low-Mg# rim) for rhyolites. The error of estimate has been minimized by probability density function analysis and corresponds to ±15 °C. We adapted the NIDIS model to evaluate the diffusive timescale (Δt) in the low-*T* resident magma (i.e., recharge band-rim interface) which represents the time spent in the last magmatic environment prior to eruption (Petrone et al., 2016).

Smoother recharge band-rim profiles are generally observed in clinopyroxenes from silicic rocks, in agreement with longer temporal intervals after mafic injection in the reservoir and prior to eruption (Fig. 9a). Conversely, steeper diffusion profiles are measured for recharge band-rim boundaries analyzed in clinopyroxene phenocrysts from more primitive products, as the result of diffusive re-equilibration of compositional zoning for shorter time periods (Fig. 9a). All timescales are summarized in Fig. 9b. Shorter timescales of ~0.1-9 years are quantified for clinopyroxenes from basalts, shoshonites, and latites, whereas longer timescales on the order of ~7-18 years and ~16-44 years are calculated for clinopyroxenes from trachytes and rhyolites, respectively (Fig. 9b). The longer crystal residence times measured for the more differentiated eruptive products are in agreement with the general increase over time of the degree of chemical evolution of magmas and the enrichment in incompatible trace elements (e.g., De Astis et al., 2013). This time-related compositional shift from basalts to rhyolites is also confirmed by the geochemical evolution of clinopyroxene core from Eruptive Epoch 5 to 8 (Fig. 6).

Mixing phenomena between high-*T* mafic and low-*T* felsic end-members are intimately related to magma dynamics recorded by the recurrent concentric zonation and dissolution texture of clinopyroxene phenocrysts, which tend to be slightly more abundant in trachyte and rhyolite (Figs. 2 and 3; Table 1). More silicic trachytes and rhyolites represent residual melts trapped-extracted from crystal mushes that are approximatively located between 5 and 10 km depth (Palummo et al., 2020). The most favorable window for crystal-melt separation occurs at a crystallinity of ~50–70% (Dufek and Bachmann, 2010), such that eruptible silicic melts can be extracted from the crystal mush, without bulk melting or remobilization of its crystalline framework (Stelten et al., 2015). Coherently, the differentiation of basalts to trachytes at Vulcano Island takes place at crystal content of ~52%, whereas the formation of highly differentiated trachytes and rhyolitic melts requires a mush system with crystallinity comprised between 59% and 84% (Palummo et al., 2020).

The compositional similarity between clinopyroxene cores and mantles + rims from trachytes and rhyolites (compare Figs. 6 and 8) suggests mutual crystallization in a colder and shallower mush region over prolonged crystal residence times (Fig. 9). The great number of recharge bands observed in silicic products, alongside resorbed cores and mottled crystals (Table 1) indicates that phenocrysts remained trapped in the mush for a prolonged period of time, thereby recording sustained injections of less differentiated magmas. Longer diffusion timescales are typically measured for phenocrysts hosted in silicic melts extracted from crystal-rich regions (Cooper, 2019). By interpolating 1) the empirical viscosity equation of Giordano et al. (2008), 2) the bulk rock analyses of products erupted at Vulcano Island (Fig. 1a), and 3) the *P*-*T*-H_2O crystallization paths of clinopyroxene-bearing magmas (Palummo et al., 2020), we found that the geochemical evolution of clinopyroxene is accompanied by an average melt viscosity increase, on the order of ~1.2 (basalt), ~2.3 (shoshonite), ~2.5 (latite), ~3.8 (trachyte), ~4.6 (rhyolite) log Pa s. In the lower crust, low viscosity basaltic magmas remain above the solidus state due to the effect of high temperature conditions. These thermal and rheological regimes allow extensive magma segregation and migration. During ascent, however, basaltic magmas cool and crystallize to develop more differentiated melts leading to the growth of clinopyroxene phenocrysts progressively more enriched in REE and HFSE (Figs. 5 and 6). In the uppermost crust, the formation of non-eruptible crystal-rich mush regions takes place by strong cooling-induced crystallization phenomena and high viscosity rhyolitic lenses develop by percolative melt transfer (Bachmann and Bergantz, 2004; Dufek and Bachmann, 2010; Masotta et al., 2016). Protracted residence times recorded by clinopyroxene phenocrysts (Fig. 9) are consistent with the tendency for phenocrysts to remain suspended in more silicic melts with a higher viscosity, as the temperature of the solidifying system decreases and the degree of crystallization increases (e.g., Hawkesworth et al., 2000 and references therein). As outlined by thermobarometric constraints (Fig. 7), after extraction of melt from the crystal mush, small-volume rhyolitic magmas stall temporarily at very shallower levels of the reservoir. Therefore, resorbed cores (Type 2), recharge bands (Type 3), and mottled resorption textures (Type 4) found in clinopyroxene phenocrysts (Figs. 2 and 3) may be also interpreted as the result of mixing between low-*T* rhyolitic magmas extracted from the crystal-rich region and fresh inputs of high-*T* free magmas rising from shoshonitic and latitic reservoirs located at moderate depths of 10-17 km (De Astis et al., 2013; Palummo et al., 2020).

5.3. Modeling magma recharge and mixing dynamics

Cr/Yb ratios measured for clinopyroxene cores, recharge bands, and mantles + rims are comparatively plotted in Fig. 10a in order to place constrain on the recharge processes and mixing dynamics governing the evolutionary history of magmas at Vulcano Island. An important aspect emerging from this comparison is the compositional diversity of clinopyroxene, characterized by decreasing Cr/Yb ratios as the geochemical evolution of magma proceeds from basalt to rhyolite (Fig. 10a). Differently from the more homogeneous chemistry of basalts erupted during the Eruptive Epoch 5, younger rhyolitic melts from Eruptive Epoch 8 were dominated by abundant crystallization of felsic minerals plus low degrees of crustal assimilation (Bullock et al., 2019; De Astis et al., 1997, 2000, 2003; Gioncada et at., 2003; Peccerillo et al., 2006). Clinopyroxene zoning patterns with highly variable Cr/Yb ratios reflect substantial chemical modifications in more silicic reservoirs due to open-system processes associated with the input of fresh magma into distinct crustal regions and related mixing and hybridization phenomena (Forni et al., 2016; Gioncada et al., 1998; Nicotra et al., 2018; Peccerillo et al., 2006; Piochi et al., 2009). Moreover, Cr/Yb ratios in clinopyroxene decrease with the sequential growth of phenocryst, from core to mantle + rim (Fig. 10a). This change validates the idea that magma mixing was likely accompanied by cooling-degassing processes, especially during the storage of magma in shallower and colder crustal regions (Mandarano et al., 2016), where the most evolved chemistry of clinopyroxene rims reflects the latest residual melt composition, immediately preceding the eruption.

With the only exception represented by the diopsidic clinopyroxene cores from basalts, there is always some degree of overlap between the trace element inventory of clinopyroxene cores, recharge bands, and mantle + rims (Fig. 10a). As schematically illustrated in Fig. 10b, the compositional heterogeneity of clinopyroxene results from the transfer of magma between different storage regions that are interconnected with each other (cf. Palummo et al., 2020). The isolated compositional group of clinopyroxene cores from basalts with extremely high Cr/Yb ratios (Fig. 10a) represent early crystal-melt equilibration in the lower crust (Fig. 10b). Conversely, the Cr/Yb ratio in clinopyroxene cores from shoshonites to rhyolites progressively decreases (Fig. 10a), in accord with the formation of more differentiated reservoirs that, however, explore continuous physico-chemical changes due to interaction between compositionally distinct magma batches (Fig. 10b).

Recharge bands in clinopyroxene phenocrysts from basalts show Cr/Yb ratios that are intermediate between those measured for clinopyroxene cores from shoshonites + latites and trachytes + rhyolites (Fig. 10a). This suggests that an early-formed crystal cargo residing in the deeper parts of the crust was remobilized and transported by mafic melts (e.g., Petrone et al., 2018; Cooper, 2019) passing through an interconnected series of differentiated magma storage regions (Fig. 10b). In a similar fashion, the occurrence of Type 4 mottled phenocrysts (i.e., aggregates of partially dissolved clinopyroxenes; Fig, 2) suggests that crystals were assembled from different parts of the crust (Fig. 10b), in agreement with analogous dynamic processes documented for clinopyroxenes erupted at Mt. Etna (Armienti et al., 2007) and Stromboli (Di Stefano et al., 2020). In this scenario, intracrystalline heterogeneities indicate a multi-stage history of magma that is characterized by mixing and hybridization phenomena operating within an articulated plumbing system (Fig. 10b), where recharge inputs encounter partially or wholly crystallized reservoirs generated by different prior magma batches. The broad compositional interval recorded by recharge bands from rhyolites (Fig. 10a) testifies to multiple inputs of mafic magma from depth, abundant cooling-induced crystallization, and protracted crystal residence times in a highly crystalline storage region.

The bulk (crystal + melt) chemical evolution of magmas points towards a unified view of cogenetic differentiation processes operating in two main magma storage regions within the crust (cf. Bachmann and Huber, 2016). The first storage region is located in lower crust near the crust-mantle boundary and is fed by primitive basalts that represent the most mafic endmembers of the differentiation series (Fig. 10b). A high-pressure crystallization assemblage develops within this lower crustal storage region (see for example Ozdemir et al., 2011). The second main storage region is located at shallower depths in the upper crust (typically between 250 and 150 MPa; see Huber et al., 2019), where magmas pond at the apex of a series of interconnected magma transfer zones (Fig.

10b). Magma dynamics at Vulcano Island are controlled by the interplay between lower and upper crust storage regions and only transient magma bodies are generated at intermediate depths (Fig. 10b), partly by mixing of magmas from these two main storage regions (Bachmann and Huber, 2016; Huber et al., 2019).

To better elucidate the clinopyroxene-related geochemical changes characterizing the eruptive history of Vulcano Island, we have investigated the evolutionary path of LREE (i.e., La) and HREE (i.e., Yb) in magmas through the partitioning model of Mollo et al. (2018, 2020b). Different equations describing the excess of strain energy (Wood and Blundy, 1997) and electrostatic energy (Wood and Blundy, 2001) are integrated in this model, in order to calculate the partitioning energetics controlling heterovalent REE cation substitutions in clinopyroxene. This makes it possible to quantify the role of clinopyroxene crystallization on the REE pattern of a magma through the estimate of a different clinopyroxene-melt partition coefficient (i.e., $D_{REE} = {}^{cpx}REE$ / ${}^{melt}REE$ on a weight basis) for each stage of crystallization. The P-T-H_2O saturation conditions of clinopyroxene phenocrysts (i.e., P = 20-750 MPa, T = 1,000-1,220 °C, and H_2O = 1.6-4.0 wt.%) that are required as input data for the partitioning modeling come from the petrological work of Palummo et al. (2020). REE cations were chosen for the modeling because of 1) the diverse but systematic zoning patterns in clinopyroxene phenocrysts, 2) the complete thermodynamic description of partitioning behavior as a function of intensive-extensive parameters, and 3) the preferential control of clinopyroxene crystallization on REE contents in the residual melt relative to other mineral phases (i.e., according to the relation between mineral weight fractions and the bulk partition coefficient; Mollo et al., 2018, 2020b). A spectrum of partition coefficients has been determined for clinopyroxene cores and recharge bands (Supplementary Material 1). Recalling the free energy exchange of the fusion reaction ${}^{cpx}REEMgSiO_2O_6 \leftrightarrow {}^{melt}REEMgSiO_2O_6$ (Wood and Blundy, 1997), the estimated values of D_{La} and D_{Yb} were used to invert the concentrations of REE in the melts from clinopyroxene cores and recharge bands (i.e., ${}^{melt}REE = {}^{cpx}REE$ / D_{REE}).

Results from calculations are plotted in Fig. 10c and compared with the bulk rock analyses of the eruptive products. Different compositional vectors (i.e., colored arrows in Fig. 10c) represent the putative REE contents of end-member magmas in equilibrium with the more homogeneous clinopyroxene cores, as calculated by the partitioning equations of Mollo et al. (2018, 2020b). These vectors are almost aligned along a common differentiation path involving the progressive increase of La-Yb contents from basalt to rhyolite. The La-Yb array resulting from partitioning modeling is divided in three distinct groups for basalts, shoshonites + latites, and trachytes + rhyolites (Fig. 10c) that roughly reflect the plumbing system architecture of Vulcano Island (Fig. 10b). The grey dashed symbols represent the putative REE contents of magmatic injections recorded by the more heterogeneous recharge bands (Fig. 10c). While most of recharge bands from basalts converge in a narrow range that is close to the compositional vector, recharge bands from trachytes and rhyolites show the largest compositional variability. This implies that the number of recharge bands and their chemical diversity axiomatically increase with increasing the silicic character of magma, thereby depicting a fan-like array indicative of open-system processes (Fig. 10c). Importantly, our modelled data set reproduce very well the bulk rock analyses of natural eruptions and their fan-like pattern (Fig. 10c). This correspondence reflects a plumbing system evolution that is persistently controlled by crystal-melt dynamics due to the interaction between different crystallizing reservoirs in which the supply of fresh magma modulates the final texture and composition of the erupted product.

We conclude that the lower crust is the most favorable location for the origin of compositionally homogeneous basaltic magmas (i.e., melt-dominated domains) and their initial stages of crystallization during transfer at intermediate depths (Fig. 10b). However, magma percolation and accumulation in the upper crustal regions lead to the formation of an interconnected series of magmatic reservoirs (i.e., crystal-dominated domains), many of which may be composed of crystal-rich mush systems (Fig. 10b). According to this conceptual model, the physical (e.g., crystallinity and melt viscosity) and chemical (e.g., degree of evolution of crystals and melts) state of magma changes dramatically in the shallowest parts of the feeding system. The discrete populations, complex compositional zoning patterns, and different residence times of clinopyroxene phenocrysts reflect the intricate crystallization history of magma. The mineral assemblage in silicic mush melts is sufficiently resilient to record numerous mafic injections and high degrees of magma mixing, hybridization, and crystallization before eruption. Taken together, the textural and compositional changes of clinopyroxene phenocrysts present a picture of a plumbing system that extends through the crust and is characterized by distributions of melts and crystals which are progressively more evolved and heterogeneous in both space and time (Fig. 10b).

6. Concluding remarks

This study illustrates the textural and compositional changes of clinopyroxene phenocrysts from basaltic to rhyolitic products erupted at Vulcano Island over a period of time from ~54 ka to 1739 CE. Phenocrysts have been categorized on the presence or absence of complex zoning patters and five distinct populations have been recognized (i.e., Type 1 homogeneous crystals, Type 2 core/resorbed cores, Type 3 recharge bands, Type 4 mottled crystals, and Type 5 sector-zoned crystals). The different growth features and intracrystalline distributions of major and trace cations in clinopyroxene closely reflect the physico-chemical changes of magma under the effects of closed- and open-system processes. By combining microanalytical data and trace element modeling, we gained useful insights into the plumbing system architecture and the intricate magmatic history of Vulcano Island. According to this approach, the following conclusions can be drawn:

1) the compositional evolution of clinopyroxene highlights that basaltic magmas are characterized by Types 1 and 2 populations, in which diopsidic cores are heralds of crystallization in the lower crust. The compositional change of clinopyroxene proceeds from diopside-augite to augite, following the polybaric-polythermal differentiation of basalts towards more differentiated melts residing in the upper crust;

2) the number of chemical heterogeneities in clinopyroxene increases in silicic eruptive products, in accord with the more frequent observation of Types 3 and 4 populations in trachytes and rhyolites. This chemical diversity reflects an open-system behavior due to injection of hotter and more primitive magmas into compositionally distinct colder and shallower reservoirs. Open-system processes are testified by multi-stage clinopyroxene dissolution phenomena that results from thermal and/or chemical disequilibrium with the recharge melt;
3) Type 5 sector-zoned crystals are typically found in shoshonites and latites. The weak sector zonation between {-1 1 1} hourglass and {*h* *k* 0} basal prism forms suggests sluggish crystallization kinetics during very slow magma ascents and/or small-scale convective transport of crystals through thermally heterogeneous magma reservoirs;
4) shorter timescales (~0.1-9 years) are quantified for clinopyroxenes from basaltic, shoshonitic, and latitic magmas, whereas longer timescales are measured for phenocrysts crystallizing in trachytic (~7-18 years) and rhyolitic (~16-44 years) reservoirs. Protracted residence times are consistent with the tendency for clinopyroxene to remain suspended in more silicic and viscous melts extracted from shallow crystal-rich regions;
5) results from partitioning modeling based on the concentrations of rare earth elements (REE) in clinopyroxene confirm the cogenetic origin for the eruptive products along a common differentiation path. Magma percolation and accumulation in the upper crustal regions lead to the formation of an interconnected series of magmatic reservoirs with different degrees of REE concentrations. Both the compositional diversity of melt and the intracrystalline heterogeneity of clinopyroxene are exacerbated in crystal-dominated mush zones, responding to the stronger diversification of REE via intense magma mixing, hybridization, and crystallization phenomena.

Acknowledgments

This work has been greatly improved by the helpful and thoughtful reviews of Andreas Klügel and one anonymous reviewer. Michael Roden is also acknowledged for his valuable editorial guidance.

References

Armienti, P., Francalanci, L., Landi, P., 2007. Textural effects of steady state behavior of the Stromboli feeding system. J. Volcanol. Geotherm. Res. 160, 86-98.

Bachmann, O., Huber, C., 2016. Silicic magma reservoirs in the Earth's crust: American Mineralogist, v. 101, p. 2377-2404.

Bachmann, O., Bergantz, G.W., 2004. On the origin of crystal-poor rhyolites: extracted from batholithic crystal mushes. J. Petrol. 45 (8), 1565-1582.

Beard, C.D., van Hinsberg, V.J., Stix, J., Wilke, M., 2019. Clinopyroxene/melt trace element partitioning in sodic alkaline magmas. J. Petrol. 60, 1797-1823. https://doi.org/10.1093/petrology/egz052.

Bergantz, G.W., Schleicher, J.M., Burgisser, A., 2015. Open-system dynamics and mixing in magma mushes. Nature Geoscience, 8(10), 793-796.

Blundy, J. D., Falloon, T. J., Wood, B. J., Dalton, J. A., 1995. Sodium partitioning between clinopyroxene and silicate melts. J. Geophys. Res. Solid Earth, 100, 15501-15515.

Bullock, L.A., Gertisser, R., O'Driscoll, B., Harland, S., 2019. Magmatic evolution and textural development of the 1739 CE Pietre Cotte lava flow, Vulcano, Italy. J. Volcanol. Geoth. Res. 372, 1-23.

Cashman, K.V., Sparks, R.S.J., Blundy, J.D., 2017. Vertically extensive and unstable crystals mushes: a unifying view of igneous processes associated with volcanoes. Science 355 (6331) eaag3055.

Clocchiatti, R., Del Moro, A., Gioncada, A., Joron, J.L., Mosbah, M., Pinarelli, L., Sbrana, A., 1994. Assessment of a shallow magmatic system: the 1888-90 eruption, Vulcano Island, Italy. Bull. Volcanol. 56, 466-486.

Cooper, K.M., 2019. Time scales and temperatures of crystal storage in magma reservoirs: Implications for magma reservoir dynamics. Philosophical Transactions of the Royal Society A, 377(2139), 20180009.

Costa, S., Masotta, M., Gioncada, A., Pistolesi, M., Bosch, D., Scarlato, P., 2020. Magma evolution at La Fossa volcano (Vulcano Island, Italy) in the last 1000 years: evidence from eruptive products and temperature gradient experiments. Contrib. Mineral. Petrol. 175 (4), 1-22.

Costa, S.; Masotta, M.; Gioncada, A.; Pistolesi, M. A Crystal Mush Perspective Explains Magma Variability at La Fossa Volcano (Vulcano, Italy). Minerals, 2021, 11, 1094. https://doi.org/10.3390/min11101094

Davì, M., De Rosa, R., Donato, P., Vetere, F., Barca, D., Cavallo, A., 2009. Magmatic evolution and plumbing system of ring-fault volcanism: the Vulcanello peninsula (Aeolian Islands, Italy). Eur. J. Mineral. 21, 1009-1028.

De Astis, G., La Volpe, L., Peccerillo, A., Civetta, L., 1997. Volcanological and petrological evolution of Vulcano Island (Aeolian Arc, southern Tyrrhenian Sea). J. Geophys. Res. 102, 8021-8050.

De Astis, G., Peccerillo, A., Kempton, P.D., La Volpe, L., Wu, T.W., 2000. Transition from calc-alkaline to potassium-rich magmatism in subduction environments: geochemical and Sr, Nd, Pb isotopic constraints from the island of Vulcano (Aeolian arc). Contrib. Mineral. Petrol. 139, 684-703.

De Astis, G., Ventura, G., Vilardo, G., 2003. Geodynamic significance of the Aeolian volcanism (Southern Tyrrhenian Sea, Italy) in light of structural, seismological, and geochemical data. Tectonics 22, 1040-1057.

De Astis, G., Lucchi, F., Dellino, P., La Volpe, L., Tranne, C.A., Frezzotti, M.L., Peccerillo, A., 2013. Geology, volcanic history and petrology of Vulcano (central Aeolian archipelago). In: Lucchi, F., Peccerillo, A., Keller, J., Tranne, C.A., Rossi, P.L. (Eds.), The Aeolian Islands Volcanoes. Geological Society, London, Memoirs vol. 37, 181-349.

Dellino, P., De Astis, G., La Volpe, L., Mele, D., Sulpizio, R., 2011. Quantitative hazard assessment of phreatomagmatic eruptions at Vulcano (Aeolian Islands, Southern Italy), as obtained by combining stratigraphy, event statistics and physical modelling. J. Volcanol. Geotherm. Res. 201, 364-384.

Di Stefano, F., Mollo, S., Ubide, T., Petrone, C. M., Caulfield, J., Scarlato, P., Nazzari, M., Andronico, D., Del Bello, E., 2020. Mush cannibalism and disruption recorded by clinopyroxene phenocrysts at Stromboli volcano: New insights from recent 2003–2017 activity. Lithos, 360, 105440.

Downes, M.J., 1974. Sector and oscillatory zoning in calcic augites from M. Etna, Sicily. Contrib. Mineral. Petrol. 47, 187-196.

Druitt, T.H., Costa, F., Deloule, E., Dungan, M., Scaillet, B., 2012. Decadal to monthly timescales of magma transfer and reservoir growth at a caldera volcano. Nature 482, 77-80.

Dufek, J., Bachmann, O., 2010. Quantum magmatism: Magmatic compositional gaps generated by melt-crystal dynamics. Geology 38 (8), 687-690.

Dunworth, E., Neumann, E.R., Rosenbaum, J., 2001. The Skien lavas, Oslo Rift: petrological disequilibrium and geochemical evolution. Contributions to Mineralogy and Petrology, 140(6), 701-719.

Ellam, R.M., Menzies, M.A., Hawkesworth, C.J., Leeman, W.P., Rosi, M., Serri, G., 1988. The transition from calc-alkaline to potassic orogenic magmatism in the Aeolian Islands, Southern Italy. Bulletin of Volcanology, 50, 386-398.

Forni, F., Ellis, B.S., Bachmann, O., Lucchi, F., Tranne, C.A., Agostini, S., Dallai, L., 2015. Erupted cumulate fragments in rhyolites from Lipari (Aeolian Islands). Contrib. Mineral. Petrol. 170, 49.

Forni, F., Bachmann, O., Mollo, S., De Astis, G., Gelman, S.E., Ellis, B.S., 2016. The origin of a zoned ignimbrite: Insights into the Campanian Ignimbrite magma chamber (Campi Flegrei, Italy), Earth and Planetary Science Letters, 449, 259-271. http://dx.doi.org/10.1016/j.epsl.2016.06.003.

Forni, F., Degruyter, W., Bachmann, O., De Astis, G., Mollo, S., 2018. Long-term magmatic evolution reveals the beginning of a new caldera cycle at Campi Flegrei. Science Advances 4 (11), eaat9401. http://dx.doi.org/10.1126/sciadv.aat9401.

Gioncada, A., Clocchiatti, R., Sbrana, A., Bottazzi, P., Massare, D., Ottolini, L., 1998. A study of melt inclusions at Vulcano (Aeolian Islands, Italy): insights on the primitive magmas and on the volcanic feeding system. Bull. Volcanol. 60, 286-306.

Gioncada, A., Mazzuoli, R., Bisson, M., Pareschi, M.T., 2003. Petrology of volcanic products younger than 42 ka on the Lipari-Vulcano complex (Aeolian Islands, Italy): an example of volcanism controlled by tectonics. J. Volcanol. Geotherm. Res. 122, 191-220.

Gioncada, A., Mazzuoli, R., Milton, A.J., 2005. Magma mixing at Lipari (Aeolian Islands, Italy): insights from textural and compositional features of phenocrysts. Journal of Volcanology and Geothermal Research, 145(1-2), 97-118.

Giordano, D., Russell, J.K., Dingwell, D.B., 2008. Viscosity of magmatic liquids: a model. Earth and Planetary Science Letters, 271(1-4), 123-134.

Giuliani, L., Iezzi, G., Mollo, S., 2020, Dynamics of volcanic systems: physical and chemical models applied to equilibrium versus disequilibrium solidification of magmas, p.101-132, in Vetere F. eds., Dynamic Magma Evolution, Geophysical Monograph Series 254, 206 pp., ISBN: 9781119521136, John Wiley & Sons Inc., New Jersey, USA. https://doi.org/10.1002/9781119521143.ch5.

Hawkesworth, C.J., Blake, S., Evans, P., Hughes, R., Macdonald, R., Thomas, L.E., Turner, S.P., Zellmer, G., 2000. Time scales of crystal fractionation in magma chambers-integrating physical, isotopic and geochemical perspectives. Journal of Petrology, 41(7), 991-1006.

Huber, C., Townsend, M., Degruyter, W., Bachmann O., 2019. Optimal depth of subvolcanic magma chamber growth controlled by volatiles and crust rheology. Nature Geoscience 12, 762–768.

Kamenetsky, V., Clocchiatti, R., 1996. Primitive magmatism of Mt. Etna: insights from mineralogy and melt inclusions. Earth Planet. Sci. Lett. 142 (3-4), 553-572.

Keller, J., 1980. The island of Vulcano. Rendiconti della Società Italiana di Mineralogia e Petrografia 3 (6), 369-414.

Kent, A.J.R., Darr, C., Koleszar, A. M., Salisbury, M.J., Cooper, K.M., 2010. Preferential eruption of andesitic magmas through recharge filtering. Nat. Geosci. 3, 631-636.

Kouchi, A., Sugawara, Y., Kashima, K., Sunagawa, I., 1983. Laboratory growth of sector zoned clinopyroxenes in the system CaMgSi2O6-CaTiAl2O6. Contributions to Mineralogy and Petrology, 83(1-2), 177-184.

Lanzafame, G., Mollo, S., Iezzi, G., Ferlito, C., Ventura, G., 2013. Unraveling the solidification path of a pahoehoe “cicirara” lava from Mount Etna volcano. Bulletin of Volcanology, 75(4), 1-16.

Le Bas, M.J., Le Maitre, R.W., Streckeisen, A., Zanettin, B., 1986. A chemical classification of volcanic rocks based on the total alkali-silica diagram. J. Petrol. 27 (3), 745-750.

Mandarano, M., Paonita, A., Martelli, M., Viccaro, M., Nicotra, E., Millar, I.L., 2016. Revealing magma degassing below closed-conduit active volcanoes: Geochemical features of volcanic rocks versus fumarolic fluids at Vulcano (Aeolian Islands, Italy). Lithos 248-251, 272-287.

Mangler, M., Petrone, C.M., Hill, S., Delgado-Granados, H., Prytulak, J., 2020. A pyroxenic view on magma hybridisation and crystallisation at Popocatépetl Volcano, Mexico. Frontiers Earth Sciences 8:362, doi: 10.3389/feart.2020.00362.

Masotta, M., Mollo, S., Freda, C., Gaeta, M., Moore, G., 2013. Clinopyroxene-liquid thermometers and barometers specific to alkaline differentiated magmas. Contrib. Mineral. Petrol. 166, 1545-1561.

Masotta, M., Mollo, S., Gaeta, M., Freda, C., 2016, Melt extraction in mush zones: The case of crystal-rich enclaves at the Sabatini Volcanic District (central Italy), Lithos, 248-251, 288-292. http://dx.doi.org/10.1016/j.lithos.2016.01.030.

Masotta, M., Pontesilli, A., Mollo, S., Armienti, P., Ubide, T., Nazzari, M., Scarlato, P., 2020. The role of undercooling during clinopyroxene growth in trachybasaltic magmas: Insights on magma decompression and cooling at Mt. Etna volcano. Geochimica et Cosmochimica Acta, 268, 258-276. https://doi.org/10.1016/j.gca.2019.10.009.

Mollo S., Putirka K., Misiti V., Soligo M., Scarlato P., 2013. A new test for equilibrium based on clinopyroxene-melt pairs: Clues on the solidification temperatures of Etnean alkaline melts at post-eruptive conditions. Chemical Geology, 352, 92-100, doi: 10.1016/j.chemgeo.2013.05.026.

Mollo S., Masotta M., 2014, Optimizing pre-eruptive temperature estimates in thermally and chemically zoned magma chambers, Chemical Geology, 368, 97-103. https://doi.org/10.1016/j.chemgeo.2014.01.007.

Mollo, S., Giacomoni, P.P., Coltorti, M., Ferlito, C., Iezzi, G., Scarlato, P., 2015. Reconstruction of magmatic variables governing recent Etnean eruptions: constraints from mineral chemistry and P-T-fO2-H2O modelling. Lithos 212-215, 311-320.

Mollo, S., Blundy, J., Scarlato, P., De Cristofaro, S.P., Tecchiato, V., Di Stefano, F., Vetere, F., Holtz, F., Bachmann, O., 2018. An integrated P-T-H2O-lattice strain model to quantify the role of clinopyroxene fractionation on REE+Y and HFSE patterns of mafic alkaline magmas: Application to eruptions at Mt. Etna. Earth Sci. Rev. 185, 32-56. https://doi.org/10.1016/j.earscirev.2018.05.014.

Mollo S., Ubide T., Di Stefano F., Nazzari M., Scarlato P., 2020a. Polybaric/polythermal magma transport and trace element partitioning recorded in single crystals: A case study of a zoned clinopyroxene from Mt. Etna. Lithos 356-357, 105382. https://doi.org/10.1016/j.lithos.2020.105382.

Mollo, S., Blundy, J., Scarlato, P., Vetere F., Holtz, F, Bachmann, O., Gaeta, M., 2020b. A review of the lattice strain and electrostatic effects on trace element partitioning between clinopyroxene and melt: Applications to magmatic systems saturated with Tschermak-rich clinopyroxenes. Earth-Science Reviews, 210, 103351. https://doi.org/10.1016/j.earscirev.2020.103351.

Nicotra, E., Giuffrida, M., Viccaro, M., Donato, P., D'Oriano, C., Paonita, A., De Rosa, R., 2018. Timescales of pre-eruptive magmatic processes at Vulcano (Aeolian Islands, Italy) during the last 1000 years. Lithos 316-317, 347-365.

Özdemir, Y., Blundy, J., Güleç, N., 2011. The importance of fractional crystallization and magma mixing in controlling chemical differentiation at Süphan stratovolcano, eastern Anatolia, Turkey. Contrib Mineral Petrol 162, 573–597. https://doi.org/10.1007/s00410-011-0613-8

Palummo, F., Mollo, S., De Astis, G., Di Stefano, F., Nazzari, M., Scarlato, P., 2020. Petrological and geochemical modeling of magmas erupted at Vulcano Island in the period 54-8 ka: Quantitative constraints on the sub-volcanic architecture of the plumbing system. Lithos, 374, 105715.

Peccerillo, A., Frezzotti, M.L., De Astis, G., Ventura, G., 2006. Modeling the magma plumbing system of Vulcano (Aeolian Islands, Italy) by integrated fluid-inclusion geobarometry, petrology, and geophysics. Geology 34 (1), 17-20.

Perinelli, C., Mollo, S., Gaeta, M., De Cristofaro, S.P., Palladino, D.M., Armienti, P., Scarlato, P., Putirka, K.D., 2016. An improved clinopyroxene-based hygrometer for Etnean magmas and implications for eruption triggering mechanisms. Am. Mineral. 101, 2774-2777.

Petrone, C.M., Bugatti, G., Braschi, E., Tommasini, S., 2016. Pre-eruptive magmatic processes re-timed using a non-isothermal approach to magma chamber dynamics. Nat. Commun. 7, 12946.

Petrone, C.M., Braschi, E., Francalanci, L., Casalini, M., Tommasini, S., 2018. Rapid mixing and short storage timescale in the magma dynamics of a steady-state volcano. Earth Planet. Sci. Lett. 492, 206-221.

Piochi, M., De Astis, G., Petrelli, M., Ventura, G., Sulpizio, R., Zanetti, A., 2009. Constraining the recent plumbing system of Vulcano (Aeolian Arc, Italy) by textural, petrological, and fractal analysis: The 1739 A.D. Pietre Cotte lava flow. Geochem. Geophys. Geosyst. 10 (No Q01009).

Putirka, K.D., 2008. Thermometers and barometers for volcanic systems. Rev. Mineral. Geochem. 69, 61-120.

Sparks, R.S.J., Sigurdsson, H., Wilson, L., 1977. Magma mixing: a mechanism for triggering acid explosive eruptions. Nature 267, 315-318.

Stelten, M.E., Cooper, K.M., Vazquez, J.A., Calvert, A.T., Glessner, J.J., 2015. Mechanisms and timescales of generating eruptible rhyolitic magmas at Yellowstone caldera from zircon and sanidine geochronology and geochemistry. Journal of Petrology, 56(8), 1607-1642.

Sun, C.G., Liang, Y., 2012. Distribution of REE between clinopyroxene and basaltic melt along a mantle adiabat: effects of major element composition, water, and temperature. Contrib. Mineral. Petrol. 163, 807-823. https://doi.org/10.1007/S00410-011-0700-X.

Sun, C., Graff, M., Liang, Y., 2017. Trace element partitioning between plagioclase and silicate melt: the importance of temperature and plagioclase composition, with implications for terrestrial and lunar magmatism. Geochim. Cosmochim. Acta 206, 273-295.

Sun, S.S., McDonough, W.F., 1989. Chemical and isotopic systematics of ocean basalts: implications for mantle composition and processes. In: Saunders, A. D., Norry, M. J. (eds) Magmatism in the Ocean Basins. Geol. Soc. Lond. Spec. Publ. 42, 313-345.

Szymanowski, D., Ellis, B.S., Wotzlaw, J.F., Buret, Y., von Quadt, A., Peytcheva, I., Bindeman, I.N., Bachmann, O., 2016. Geochronological and isotopic records of crustal storage and assimilation in the Wolverine Creek-Conant Creek system, Heise eruptive centre, Snake River Plain. Contributions to Mineralogy and Petrology, 171(12), 1-15.

Tecchiato, V., Gaeta, M., Mollo, S., Scarlato, P., Bachmann, O., Perinelli, C., 2018. Petrological constraints on the high-Mg basalts from Capo Marargiu (Sardinia, Italy): Evidences of cryptic amphibole fractionation in polybaric environments, Journal of Volcanology and Geothermal Research, 349, 31-46. https://doi.org/10.1016/j.jvolgeores.2017.09.007.

Ubide, T., Kamber, B.S., 2018. Volcanic crystals as time capsules of eruption history. Nat. Commun. 9, 326.

Ubide, T., Mollo, S., Zhao, J.-X., Nazzari, M., Scarlato, P., 2019a. Sector-zoned clinopyroxene as a recorder of magma history, eruption triggers, and ascent rates. Geochimica et Cosmochimica Acta, 251, 265-283. https://doi.org/10.1016/j.gca.2019.02.021.

Ubide, T., Caulfield, J., Brandt, C., Bussweiler, Y., Mollo, S., Di Stefano, F., Nazzari, M., Scarlato, P., 2019b. Deep Magma Storage revealed by Multi-Method Elemental Mapping of Clinopyroxene Megacrysts at Stromboli Volcano. Frontiers in Earth Science, 7:239. https://doi.org/10.3389/feart.2019.00239.

Ventura, G., 2013. Kinematics of the Aeolian volcanism (Southern Tyrrhenian Sea) from geophysical and geological data. In: Lucchi, F., Peccerillo, A., Keller, J., Tranne, C.A., Rossi, P.L. (Eds.), The Aeolian Islands Volcanoes. Geological Society, London, Memoirs 37, 3-11.

Welsch, B., Hammer, J., Baronnet, A., Jacob, S., Hellebrand, E., Sinton, J., 2016. Clinopyroxene in postshield Haleakala ankaramite: 2. Texture, compositional zoning and supersaturation in the magma. Contrib. Mineral. Petrol. 171, 6. https://doi.org/10.1007/s00410-015-1213-9.

Welsch, B., Faure, F., Bachèlery, P., Famin, V., 2009. Microcrysts record transient convection at Piton de la Fournaise volcano (La Réunion hotspot). Journal of Petrology, 50(12), 2287-2305.

Wood, B.J., Blundy, J.D., 1997. A predictive model for rare earth element partitioning between clinopyroxene and anhydrous silicate melt. Contrib. Mineral. Petrol. 129, 166-181. https://doi.org/10.1007/s004100050330.

Wood, B.J., Blundy, J.D., 2001. The effect of cation charge on crystal–melt partitioning of trace elements. Earth Planet. Sci. Lett. 188, 59-71. https://doi.org/10.1016/S0012-821X(01)00294-1.

Zanon, V., Frezzotti, M.L., Peccerillo, A., 2003. Magmatic feeding system and crustal magma accumulation beneath Vulcano Island (Italy): evidence from fluid inclusion in quartz xenoliths. J. Geophys. Res. 108, 2298-2301.

Figure captions

Fig. 1. Schematic map of Vulcano Island showing the locations of rock samples that are the subject of the present study (a). The map legend refers to Eruptive Epochs from 1 to 8, as reported in De Astis et al. (2013). Total alkali vs. silica (TAS) diagram after Le Bas et al. (1986) (b). The rock samples are classified as basalts, basaltic trachyandesites (shoshonites), trachyandesites (latites), trachytes, and rhyolites.

Fig. 2. Back-scattered electron (BSE) photomicrographs showing the most important textural features of clinopyroxene phenocrysts: Type 1 homogeneous crystals, Type 2 core/resorbed cores, Type 3 recharge bands, Type 4 mottled crystals, and Type 5 sector-zoned crystals.

Fig. 3. Electron microprobe intensity maps showing chemical zonation patterns of Type 2 core/resorbed cores, Type 3 recharge bands, and Type 5 sector-zoned crystals. For Type 3 recharge bands, note the development of Cr-rich concentric growth zones on early-formed clinopyroxene cores, within the clinopyroxene mantle, and at the clinopyroxene rim.

Fig. 4. Compositional ranges of clinopyroxene cores and mantles + rims are compared with the recharge bands. The Mg-number [Mg# = X_{Mg} / (X_{Mg} + X_{Fe2+}), where X is the cation fraction and all iron is expressed as Fe^{2+}] of clinopyroxene is plotted against the sum of diopside + hedenbergite components (i.e., ΣDiHd) and the concentration of TiO_2.

Fig. 5. Chondrite- (a) and primordial mantle- (b) normalized patterns of trace elements in clinopyroxene cores and mantles + rims. Normalization data are from Sun and McDonough (1989).

Fig. 6. Trace element patterns in clinopyroxene cores are compared with those from recharge bands. Elements have been selected in order to represent different geochemical groups: 1) light rare earth elements (LREE; Ce and Eu), 2) heavy rare earth elements (HREE; Yb), 3) high field strength

elements (HFSE; Zr), and 4) transition elements (TE; Cr and V). The Eu anomaly has been calculated as Eu/Eu* = Eu_N / (Sm_N × Gd_N)$^{0.5}$, where the subscript N indicates element concentrations normalized to the chondrite analysis reported in Sun and McDonough (1989).

Fig. 7. *P* and *T* histograms obtained by clinopyroxene-based barometric and thermometric calculations performed by equilibrating clinopyroxene core and bulk rock compositions as described in Palummo et al. (2020).

Fig. 8. Trace element patterns in clinopyroxene mantles + rims are compared with those from recharge bands. Elements have been selected in order to represent different geochemical groups: 1) light rare earth elements (LREE; Ce and Eu), 2) heavy rare earth elements (HREE; Yb), 3) high field strength elements (HFSE; Zr), and 4) transition elements (TE; Cr and V). The Eu anomaly has been calculated as Eu/Eu* = Eu_N / (Sm_N × Gd_N)$^{0.5}$, where the subscript N indicates element concentrations normalized to the chondrite analysis reported in Sun and McDonough (1989).

Fig. 9. Grey value diffusion profiles of two representative clinopyroxene crystals from shoshonite and rhyolite products (a). The diffusion profiles were calculated inside the blue area in the red box of the associated back-scattered electron (BSE) microphotograph. The analytical data set was modelled using the NIDIS code of Petrone et al. (2016) to quantify the time (Δt) elapsed between recharge band and the onset of eruption. Summary of all the time scales estimated through the application of NIDIS to clinopyroxene phenocrysts (b). Error bars represent minimum and maximum Δt uncertainties from NIDIS modeling.

Fig. 10. Cr/Yb ratios measured for clinopyroxene cores, recharge bands, and mantles + rims are comparatively displayed in order to place constraints on the recharge processes and mixing dynamics governing the evolutionary history of magmas (a). Working model for the extended plumbing system at Vulcano Island and the dynamic growth of clinopyroxene from magmas

exploring continuous physico-chemical changes due to the presence of interconnected reservoirs (b). Results from calculations based on the partitioning model of Mollo et al. (2018, 2020b) (c). The estimated values of La and Yb partitioning were used to invert the concentrations of REE in the melts from clinopyroxene cores and recharge bands. Different compositional vectors (i.e., colored arrows) represent the putative REE contents of end-member magmas in equilibrium with the more homogeneous clinopyroxene cores. The grey dashed symbols represent the putative REE contents of magmatic injections recorded by the more heterogeneous recharge bands.

Figure 1

Click here to access/download;Figure;Fig.01.jpg

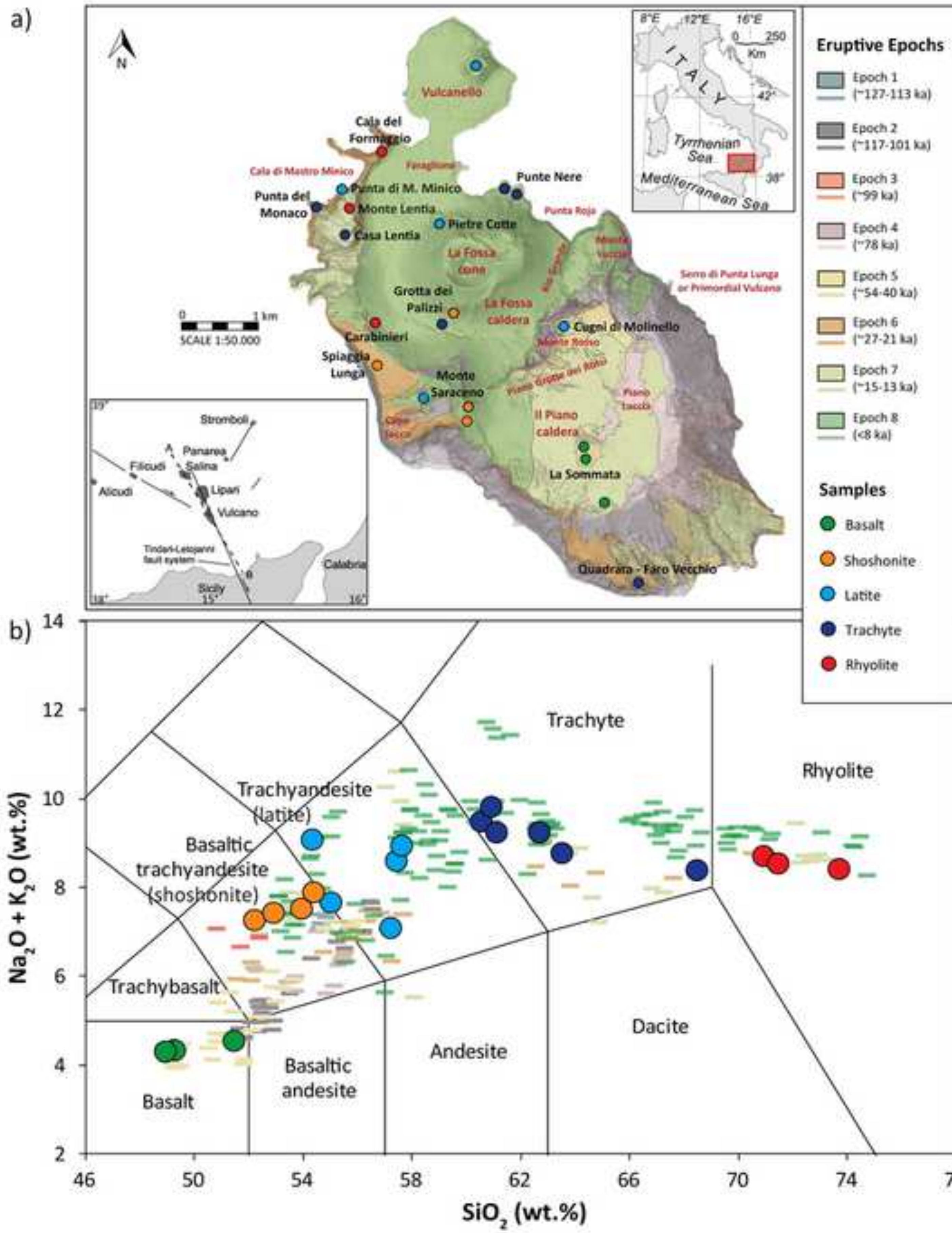

Figure 2

Click here to access/download;Figure;Fig.02.jpg

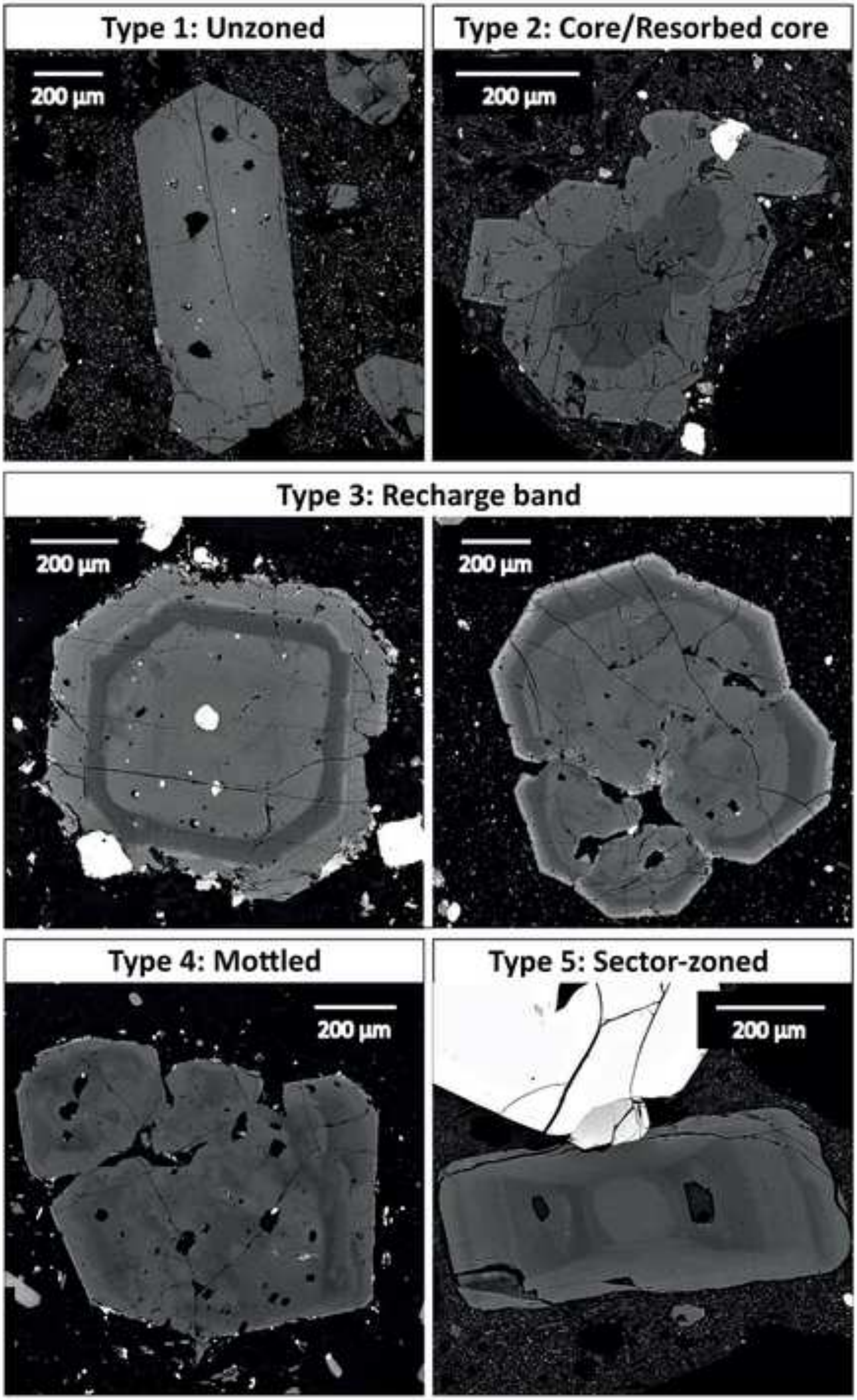

Figure 3

Click here to access/download;Figure;Fig.03.jpg

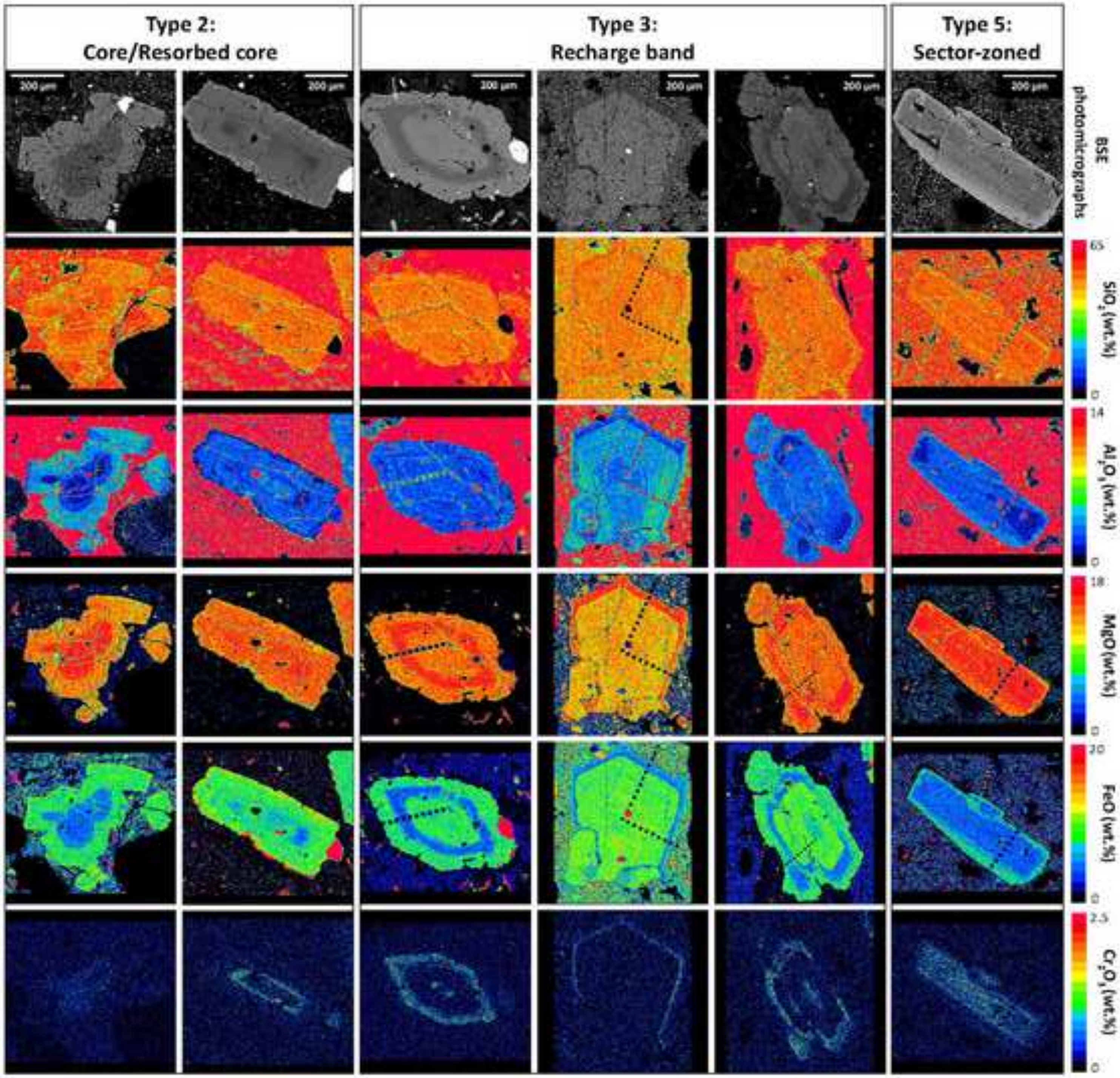

Figure 4

Click here to access/download;Figure;Fig.04.jpg

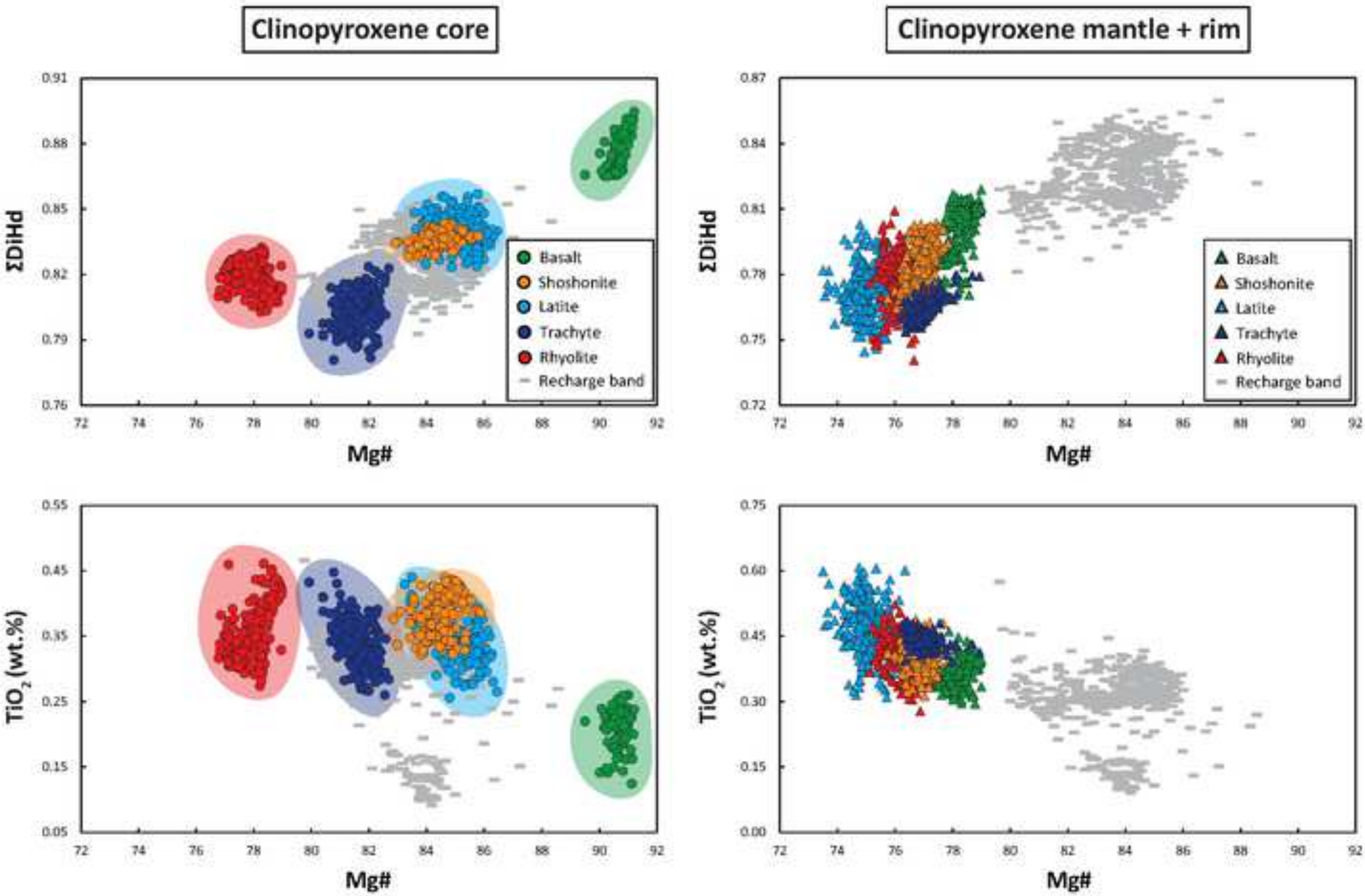

Figure 5

Click here to access/download;Figure;Fig.05.jpg

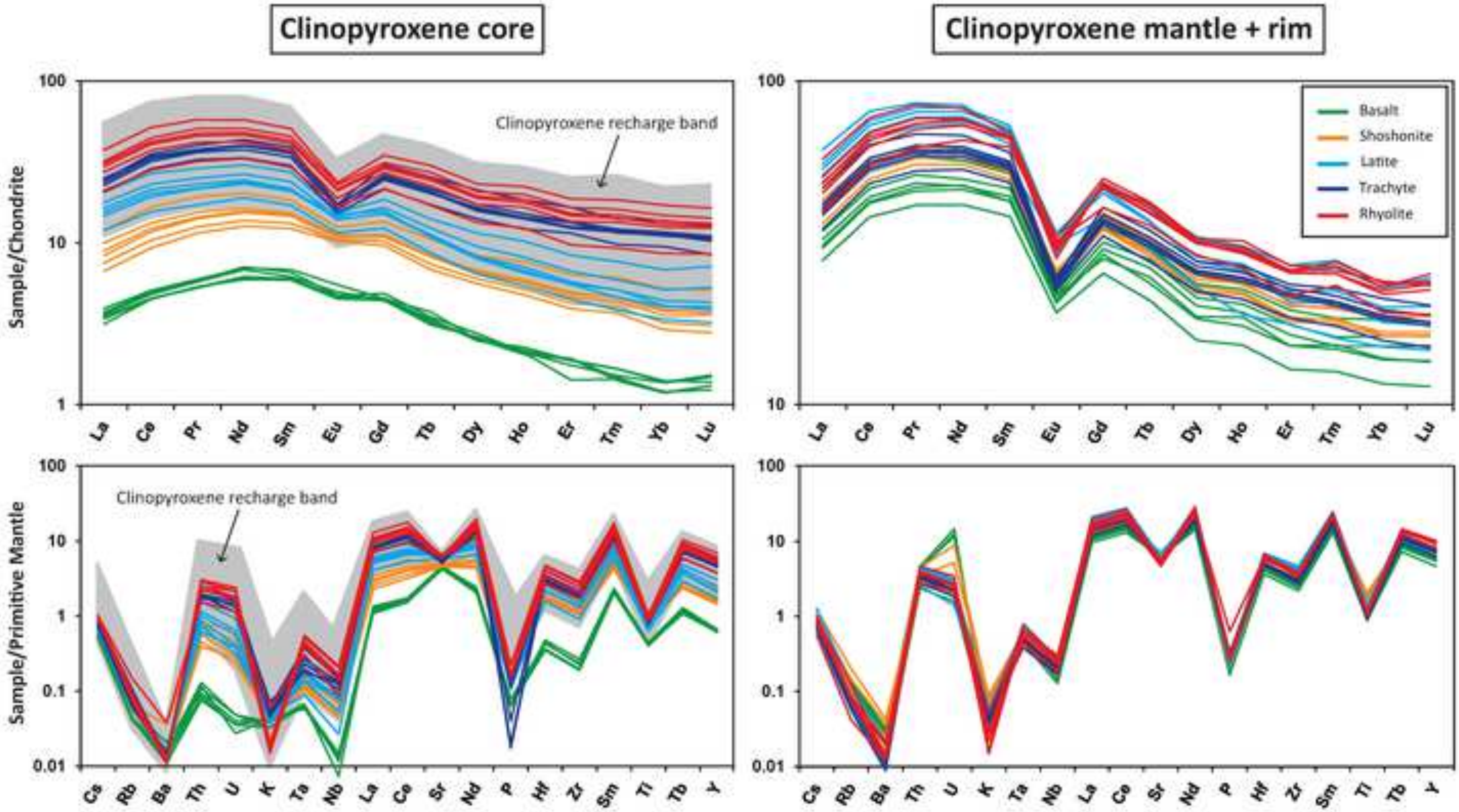

Figure 6

Click here to access/download;Figure;Fig.06.jpg

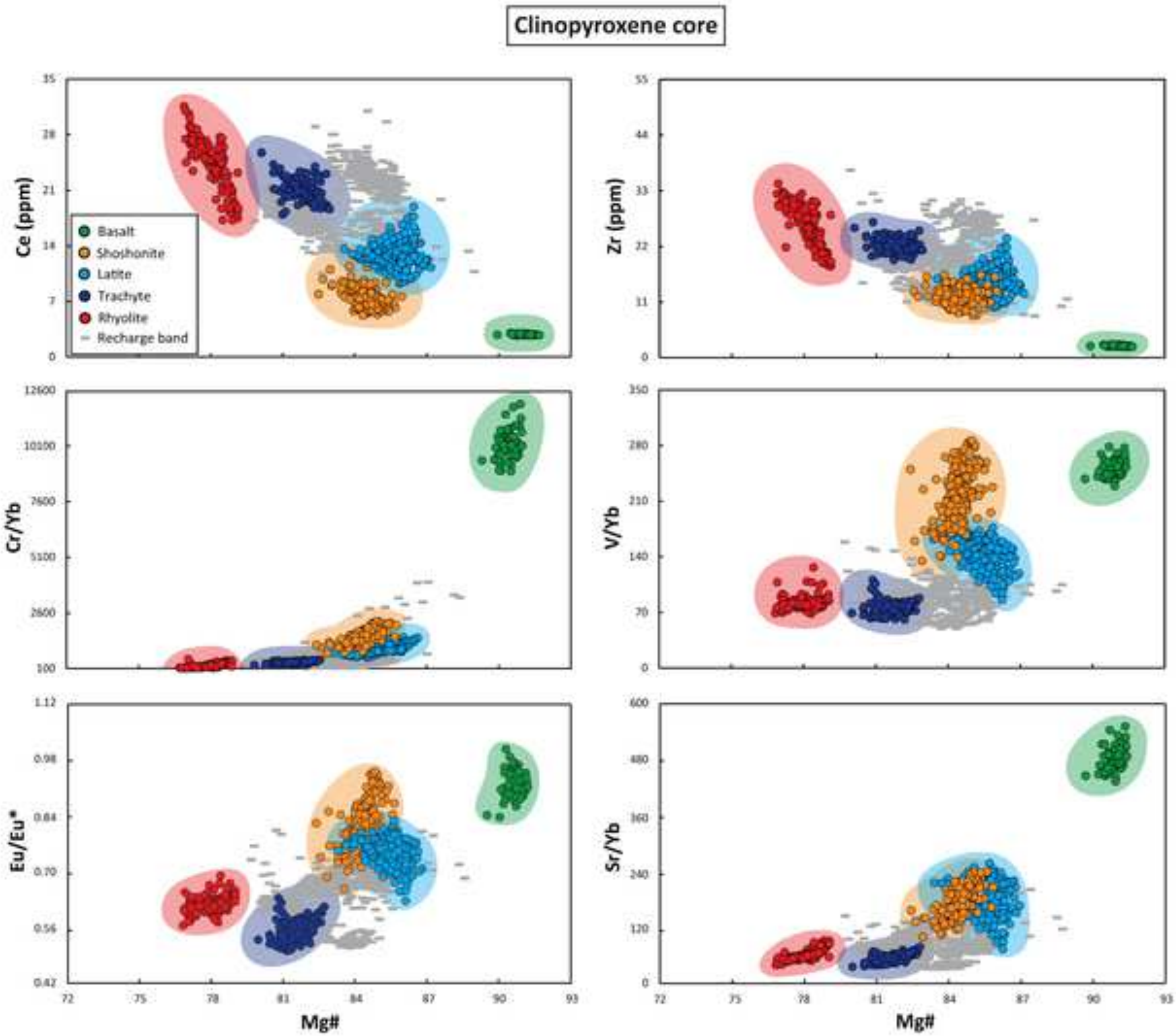

Figure 7

Click here to access/download;Figure;Fig.07.jpg

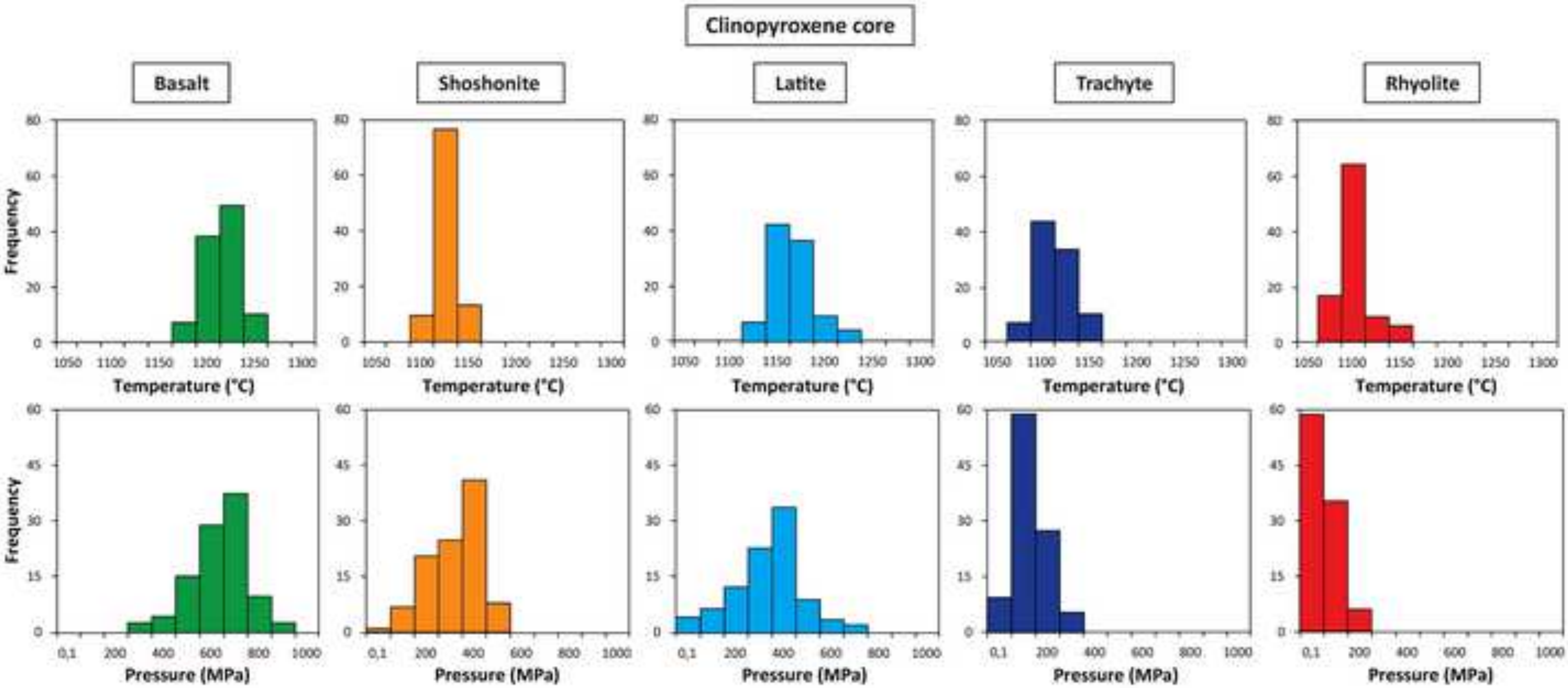

Figure 8

Click here to access/download;Figure;Fig.08.jpg

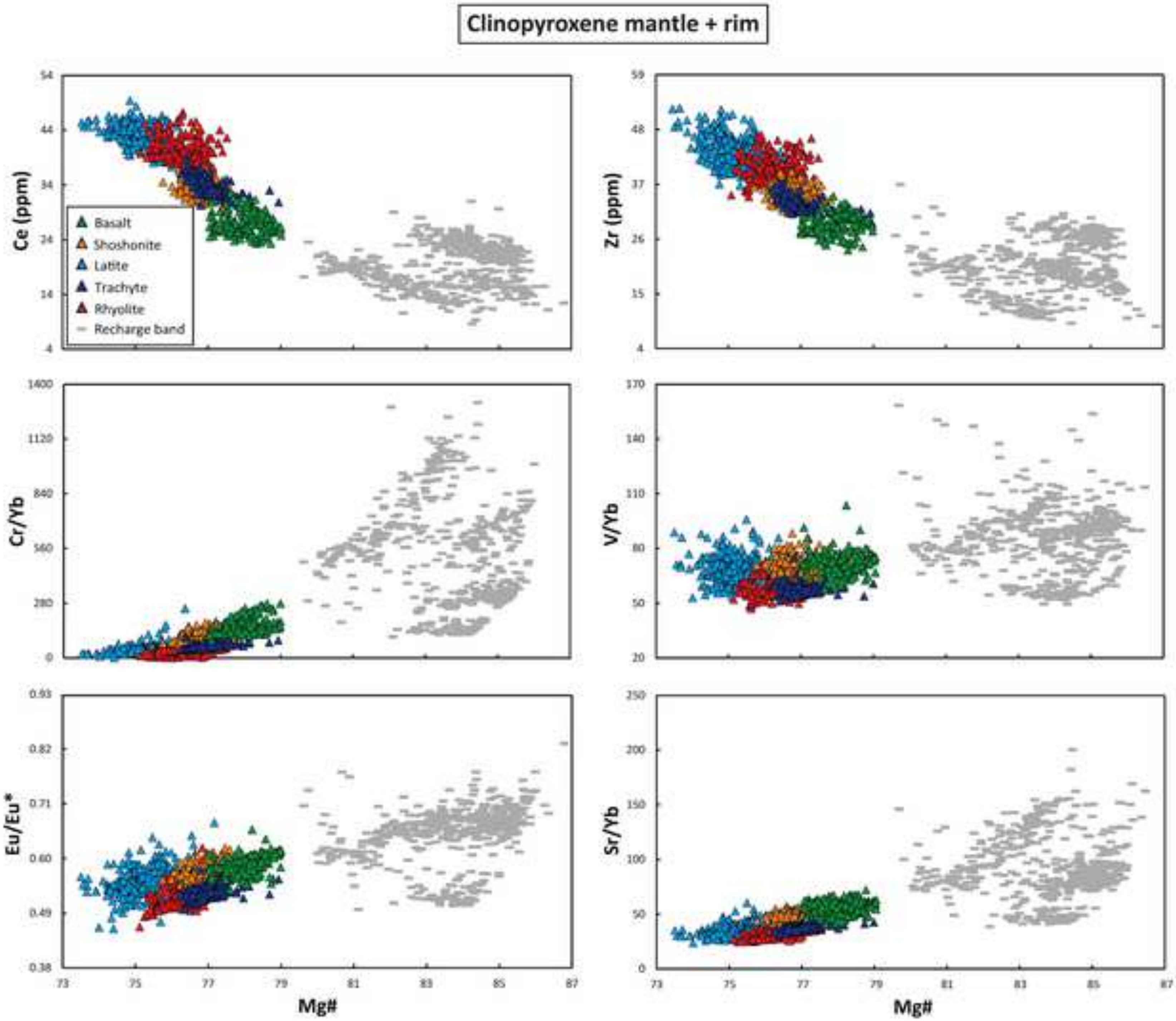

Figure 9 Click here to access/download;Figure;Fig.09.jpg

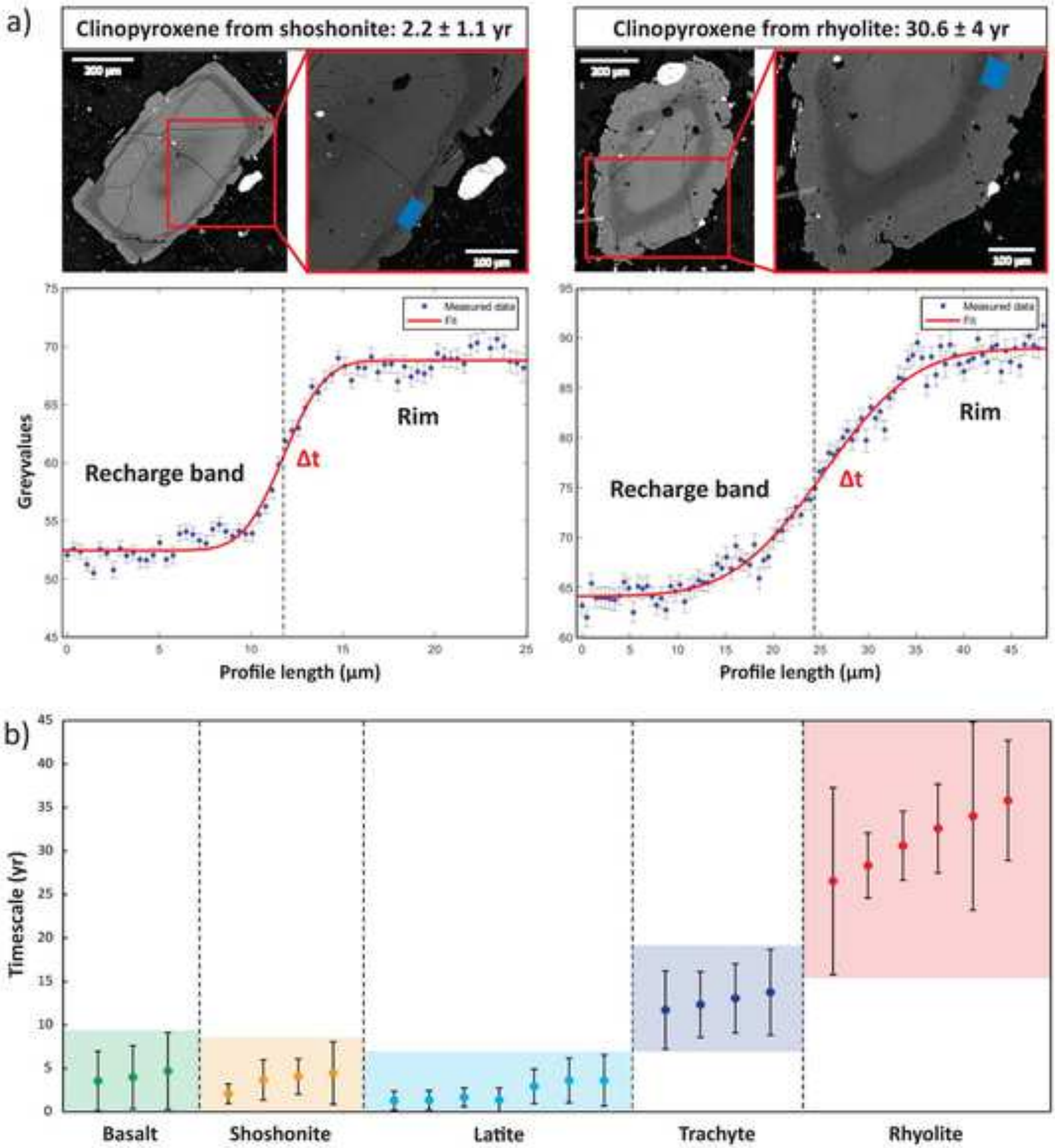

Figure 10

Click here to access/download;Figure;Fig.10.jpg

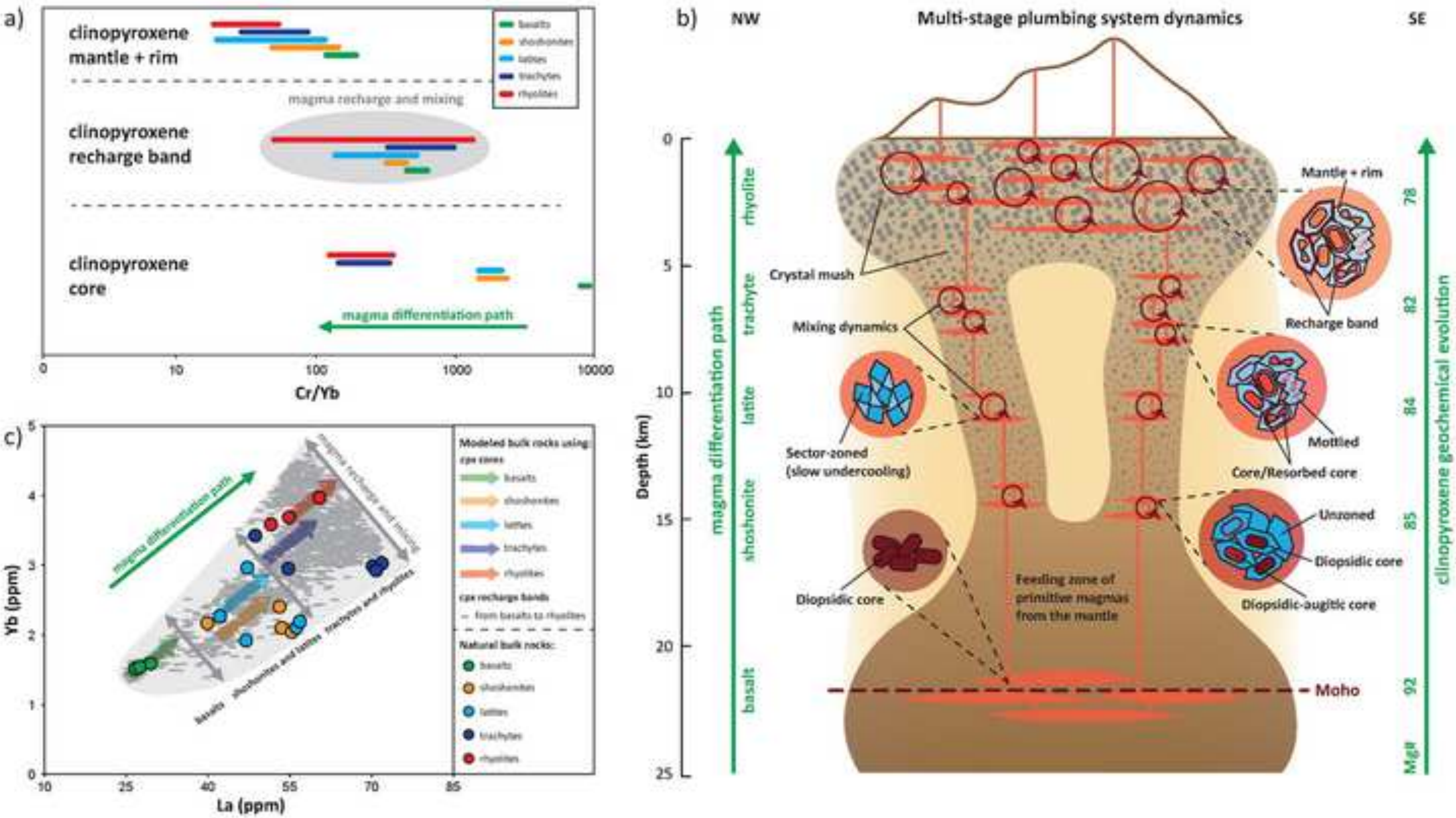

Table 1. Texturel features of clinopyroxene phenocrysts from basalts to rhyolites erupted at Vulc

	Host rock	**Basalt**	**Basalt**
	Eruptive Epoch	5	5
	Formation	La Sommata	La Sommata
	Sample	*VL168/2*	*VL 168/12*
Number of observations for each rock sample	Type 1: unzoned crystals	9	8
	Type 2: cores/resorbed cores	7	8
	Type 3: recharge bands	-	6
	Type 4 : mottled crystals	-	-
	Type 5: sector-zoned crystals	-	-
	Host rock	**Latite**	**Trachyte**
	Eruptive Epoch	8	6
	Formation	Pietre Cotte	Punta del Monaco
	Sample	*VL339/1*	*VL175C/3*
	Type 1: unzoned crystals	-	-
	Type 2: cores/resorbed cores	10	11
	Type 3: recharge bands	11	11
	Type 4 : mottled crystals	6	8
	Type 5: sector-zoned crystals	6	-

cano Island in the last ~54 ka

Basalt	Shoshonite	Shoshonite	Shoshonite	Shoshonite
5	6	8	8	8
La Sommata	Spiaggia Lunga	Monte Saraceno	Monte Saraceno	Grotta dei Palizzi
VL 194/1	*VL230/7*	*VL209A/2*	*VL180*	*VL90/1*
9	7	6	-	-
7	7	8	9	8
6	7	8	8	9
-	6	6	7	6
-	6	6	6	6
Trachyte	**Trachyte**	**Trachyte**	**Trachyte**	**Trachyte**
6	7	8	8	8
Quadrara	Casa Lentia	Punte Nere	Punte Nere	Grotta dei Palizzi
VL229/6	*VL183/10*	*VLPNa*	*VLPNb*	*VLPA*
-	-	-	-	-
10	10	11	10	11
12	11	12	11	12
8	8	8	9	9
-	-	-	-	-

Latite	**Latite**	**Latite**	**Latite**
6	7	8	8
Mastro Minico	Cugni di Molinello	Monte Saraceno	Vulcanello
VL175B/1	*VL144/2*	*VL213B/2*	*VL286*
-	-	-	-
8	9	10	11
10	10	10	10
7	6	7	6
7	7	6	6
Rhyolite	**Rhyolite**	**Rhyolite**	
6	7	8	
Cala del Formaggio	Monte Lentia	Carabinieri	
VL182/1	*VL178/11A*	*VL181*	
-	-	-	
12	12	13	
13	12	12	
10	10	9	
-	-	-	